J. Fluid Mech. (2021), *vol*. 911, A9, doi:10.1017/jfm.2020.1018

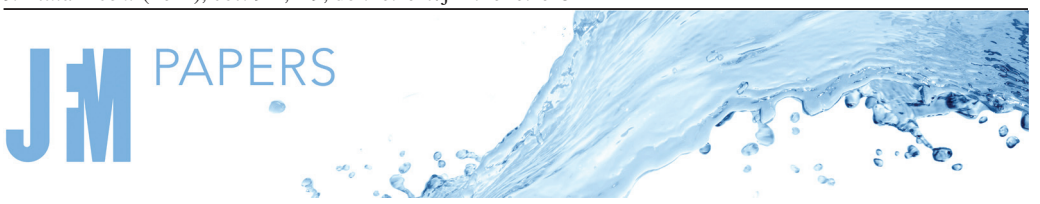

Parametrization of irreversible diapycnal diffusivity in salt-fingering turbulence using DNS

Yuchen Ma[1],† **and W. R. Peltier**[1]

[1]Department of Physics, University of Toronto, 60 St George Street, Toronto, ON, M5S 1A7, Canada

(Received 20 April 2020; revised 21 August 2020; accepted 8 November 2020)

We employ direct numerical simulations of salt fingering engendered turbulent mixing to derive a parameterization scheme for the representation of this physical process in low-resolution ocean models and compare the results with those previously suggested on empirical grounds. In this analysis we differentiate between the reversible and irreversible contributions to diapycnal diffusivity associated with the turbulence generated by this mechanism. The necessity of such a distinction has been clearly recognized in connection with shear-driven density stratified turbulence processes: only irreversible processes can contribute to the effective turbulent diapycnal diffusivity. We expand the formalism herein to the more complicated salt-fingering case as a first step towards analysis of the general case. The irreversible fluxes are determined in the case of salt fingering related turbulence by examining high-resolution direct numerical simulation (DNS)-derived turbulence data sets based upon two different models: namely the 'unbounded gradient model' and the 'interface model' with depth-dependent gradients of temperature and salinity. By fitting the irreversible diapycnal fluxes in the unbounded gradient model (for equilibrium states) as a function of density ratio (the governing non-dimensional parameter), we derive a functional form that can be used as a basis for a next generation salt-fingering parametrization scheme. By applying this scheme to the interface model, we demonstrate that the local fluxes predicted agree well with those obtained from the numerical simulations based upon this more complex model. We compare this new DNS-derived turbulence parameterization with those that have been derived empirically.

Key words: double diffusive convection, transition to turbulence, turbulent mixing

1. Introduction

Salt-fingering derived convective turbulence often develops in the equatorial ocean environment where warmer salty water lies above relatively cold and fresh water. The micro-scale fingering structures can significantly enhance the local vertical mixing rate,

† Email address for correspondence: zaizai12510@gmail.com

whose influence must be parametrized on the coarse grid of a typical global-scale ocean model. In the ocean component of most global climate models (see Smith *et al.* (2010), Griffies *et al.* (2015) for example), the currently implemented parametrization scheme for salt fingering induced vertical mixing is based on empirical fitting to the measurements made in the context of the North Atlantic tracer release experiment (NATRE) (St. Laurent & Schmitt 1999). In the interpretation of ocean measurements of this kind (see a recent review of Nakano & Yoshida (2019)), the (perhaps strong) influence of shear-driven turbulence to the inferred net vertical mixing has to be removed in order to obtain an accurate estimate of the contribution of salt fingering engendered turbulence to turbulent diffusivity (see St. Laurent & Schmitt (1999), Inoue *et al.* (2007) for example), which inevitably leads to large error bars in parametrized values. At the same time, diffusivities can only be accurately parametrized for regions of the parameter space that are actually sampled by the observations, and the majority of the available data sets appear to be confined to the relatively narrow range $1.3 < R_\rho < 2$ (in which the density ratio R_ρ is defined as $\alpha\Theta_z/\beta S_z$ where Θ, S are potential temperature and salinity, and α,β are the thermal expansion rate and haline contraction rate, respectively).

These difficulties may be effectively eliminated by recourse to reliance upon the results of the direct numerical simulation (DNS) of the mixing process, if it is possible to generate the turbulence data sets required in the regions of parameter space in which the parameterization is to be applied. If this condition can be satisfied, which will often involve significant computational investment, the fluxes engendered by the turbulence may be employed directly in the definition of an appropriate parameterization scheme. The micro-scale nature of salt-fingering instability makes the computational load for such simulations quite demanding. In fact, the required three-dimensional simulations have become available only in the last decade due to the increase of computation power required to produce the needed analyses. In the existing published record of work in this area, two different models have been primarily employed in simulations of the salt-fingering process. The first model configuration to be employed in such analyses is the so-called 'unbounded gradient model' (named and reviewed in chapter 3 of the book of Radko (2013)), in which 'homogeneous' salt fingering is simulated in uniform vertical background gradients of temperature and salinity. High-resolution three dimensional simulations using this model (for example Traxler *et al.* 2011; Radko & Smith 2012) demonstrate that the turbulence so engendered evolves into a statistically stable equilibrium state. The equilibrium vertical fluxes of heat and salt delivered by such simulations have been fit as a function of R_ρ by Radko & Smith (2012), thereby leading to an initial purely DNS-based parametrization of salt-fingering turbulence in the range $1 < R_\rho < 3$. The second model to be employed in the simulation of salt-fingering turbulence is the so-called 'interface model' (or 'two-layer' model, as also reviewed in Radko (2013)) in which two well-mixed layers are separated by a smooth but localized interface. In this model salt fingers are observed to grow from the midpoint of the interface and extend into the margins of the transition layer. Kimura, Smyth & Kunze (2011) employed this model to study salt-fingering fluxes under the combined action of shear and salt-fingering instability. They employed the average of fluxes over the interface region in a quasi-equilibrium state of the system to parametrize the fluxes as a function of both the density ratio R_ρ and gradient Richardson number Ri (a primary control variable in shear generated stratified flow turbulence). Since both models can be employed as a basis for the inference of fluxes of heat and salt, it is natural to enquire as to which model might be expected to provide the most useful data for the understanding of salt-fingering fluxes in the actual oceanographic environment, in which the ratio of the diffusivity for salt to that for heat, τ say, has the very low value of 0.01. In the present paper our intention is to re-examine the relationship between these

two models by performing direct numerical simulations for both across a wide range of the parameter space ($1 < R_\rho < 10$) using both the unbounded gradient model and large domain simulations with the interface model.

A further important aspect in the analyses to be discussed in what follows is that we will differentiate between the reversible and irreversible contributions to the diapycnal fluxes of heat and salt in salt-fingering convection. Although the necessity of such a distinction has been clearly recognized in shear-driven stratified turbulence processes (e.g. Caulfield & Peltier 2000; Peltier & Caulfield 2003), little attention has been paid to the possibility of its importance in double-diffusive mixing. In shear-driven stratified turbulence the total potential energy must be divided into available potential energy and background potential energy as only a portion of the total potential energy of the system is actually available for conversion into kinetic energy. In this case, mixing efficiency is usually of the order of 20 % (estimated in Osborn (1980) but Mashayek & Peltier (2013) and Mashayek, Caulfield & Peltier (2017) demonstrate that this value of mixing efficiency may often be significantly exceeded), as irreversible dissipative processes appear solely as a continuous increase of the background potential energy. The large-scale stirring of the fluid on the scale of individual 'billows' is entirely reversible (Winters *et al.* 1995). In the problem of shear-driven stratified turbulence, furthermore, the background potential energy of the system is associated with the potential energy of an adiabatic rearrangement of fluid parcels such that the density is monotonically decreasing with height. This definition guarantees that the background potential energy can only increase (in a closed system) by diffusion on the molecular scale which irreversibly modifies the densities of neighbouring fluid parcels, and, thus, constitutes an irreversible flux.

Such distinctions have not yet been applied to the double-diffusive system either in the presence or absence of shear. In the present paper we will focus on the case without shear as a necessary first step towards analysis of the general case. Although we will find the necessity of this distinction to be modest in the absence of shear, we will demonstrate that it plays an important role in out of equilibrium circumstances. In numerical simulations doubly diffusive fluxes continue to be estimated using the traditional definition of heat flux $\overline{w'\Theta'}$ (or $\overline{w'S'}$ for salt flux, where the overbar represents a horizontal average and the prime indicates the difference between a field value and its horizontal average) in which the fluxes so defined include both reversible and irreversible components (see Traxler *et al.* (2011), Kimura *et al.* (2011) for example). However, the analyses of the distinction between reversible and irreversible fluxes in the shear-driven stratified turbulence case cannot be directly applied to the double-diffusive system. As we will show, the critical idea needed to separate reversible from irreversible processes in the double diffusion case involves separation of the background potential energy into a background potential energy associated with temperature and a background potential energy associated with salinity. These distinct background potential energies will be shown to be related to irreversible heat and salt fluxes, respectively. It is worth noting that the background potential energies defined in the current work differ from the definitions employed in the recent work of Middleton & Taylor (2020). In this work the original formulae for background potential energy in Winters *et al.* (1995) are retained in the double-diffusion case, which therefore continues to rely on sorting the density field itself. After introducing the revised methodology that is required for analysis of doubly diffusive mixing, we will provide a detailed comparison of these two theoretical frameworks to demonstrate that accurate identification of the irreversible heat and salt fluxes require application of the new formalism we have developed.

In the present paper we will investigate, using the results of our DNS turbulence simulations, the distinction between reversible and irreversible fluxes in direct numerical simulations of turbulence in both the unbounded gradient model and the interface model. Our analyses of salt fingering engendered turbulence will show that, while the irreversible heat flux remains very close to that predicted using the traditional definition $\overline{w'\Theta'}$, the irreversible salt flux is strongly influenced by the disruption of individual salt fingers (by the secondary zig-zag instability of Holyer (1984)) rather than salt-finger growth. This causes a clear phase lag between the temporal evolution of $\overline{w'S'}$ and the irreversible salt flux in the evolution of salt-fingering fields. Once the system has entered the statistical equilibrium state, however, the irreversible fluxes will be shown to be closely consistent with traditional fluxes. As a result, the existing theories based on the flux-gradient laws based upon the traditional definitions (e.g. Radko 2003; Stellmach *et al.* 2011) remain essentially unaltered by insisting that they be determined solely on the basis of the irreversible fluxes.

The outline of this paper will proceed as follows. In § 2 we will briefly review the characteristics of both the unbounded gradient model and the interface model. The energy budget analyses for both models are also discussed in § 2 in which we will describe the detailed manner in which the distinction must be made between irreversible and reversible processes in a doubly diffusive system in the absence of shear. After a brief discussion of the numerical methodologies employed as a basis for our direct numerical simulations in § 3, the results obtained from these simulations are presented in § 4, in which we will illustrate the relationships between the unbounded gradient model and the interface model. Section 4 also includes detailed verification of the formal budget analyses described in § 2 as well as a detailed comparison between the traditionally defined fluxes for both model problems and those defined in terms of the irreversible fluxes alone. In § 5 we will discuss how these irreversible fluxes may be employed in salt-fingering turbulence parametrization schemes. A summary and conclusions are offered in § 6.

2. Irreversible fluxes in salt-fingering systems

In this section we describe the formalism required to extend the notion of irreversible mixing to the salt-fingering system. As these fluxes must be calculated differently for the two different models we intend to discuss, we will firstly provide a brief review concerning the physical settings of the two models.

2.1. *The unbounded gradient model and the interface model*

Depending on the different initial and boundary conditions in simulations of the salt-fingering system, the evolution of the fingering field can vary considerably. In fact, three different representations (the unbounded gradient model, the interface model and the bounded gradient model) have been employed by different researchers to discuss different aspects of salt-fingering instabilities and these have been summarized in Radko (2013). The unbounded gradient model and interface model, which we will employ herein to calibrate and test the turbulent flux laws, will be briefly reviewed in this subsection in order to fix ideas.

The nonlinear hydrodynamic field equations for the heat-salt doubly diffusive system are

$$\frac{\mathrm{D}u}{\mathrm{D}t} = -\frac{1}{\rho_0}\frac{\partial p'}{\partial x} + \nu\nabla^2 u, \tag{2.1a}$$

$$\frac{\mathrm{D}v}{\mathrm{D}t} = -\frac{1}{\rho_0}\frac{\partial p'}{\partial y} + \nu\nabla^2 v, \tag{2.1b}$$

$$\frac{\mathrm{D}w}{\mathrm{D}t} = -\frac{1}{\rho_0}\frac{\partial p'}{\partial z} - g\frac{\rho-\rho_0}{\rho_0} + \nu\nabla^2 w, \tag{2.1c}$$

$$\boldsymbol{\nabla}\cdot\boldsymbol{u} = 0, \tag{2.1d}$$

$$\frac{\mathrm{D}\Theta}{\mathrm{D}t} = \kappa_\theta\nabla^2\Theta, \tag{2.1e}$$

$$\frac{\mathrm{D}S}{\mathrm{D}t} = \kappa_s\nabla^2 S, \tag{2.1f}$$

$$\rho = \rho_0(1-\alpha(\Theta-\Theta_0)+\beta(S-S_0)). \tag{2.1g}$$

In these field equations the velocity vector field is $\boldsymbol{u}(x, y, z, t) = \{u, v, w\}$, the potential temperature field is $\Theta(x, y, z, t)$ and the salinity field is $S(x, y, z, t)$. In the linear equation of state (2.1*g*), the thermal expansion rate α and salinity contraction coefficient β are both assumed to be constant. In this system, $p'(x, y, z, t)$ is the deviation of the pressure from a background state of hydrostatic balance, and ν,κ_θ and κ_s are kinematic viscosity and molecular diffusivity for heat and for salt, respectively, in the advection–diffusion equations ((2.1*e*) and (2.1*f*)).

Equation (2.1) are the governing equations for both the unbounded gradient model and the interface model. The major distinction between these models concerns the different initial and boundary conditions to be applied. The unbounded gradient model is depicting salt-fingering fields in a homogeneous environment with constant background temperature gradient Θ_{z0} and salinity gradient S_{z0}, and so the initial conditions are

$$\Theta(x, y, z) = \Theta_{z0}z, \tag{2.2a}$$

$$S(x, y, z) = S_{z0}z, \tag{2.2b}$$

in which $\Theta_{z0} = \Delta\Theta/L$ and $S_{z0} = \Delta S/L$, as illustrated in figure 1(*a*). The boundary conditions for velocity as well as for the perturbation fields Θ' and S' (defined as deviations from the horizontally uniform-gradient profiles) are periodic in all three coordinate directions. Specifically, the vertical boundary conditions for Θ and S are

$$\Theta(x, y, z = L, t) = \Theta(x, y, z = 0, t) + \Delta\Theta, \tag{2.3a}$$

$$S(x, y, z = L, t) = S(x, y, z = 0, t) + \Delta S. \tag{2.3b}$$

By applying these vertical boundary conditions, we may treat the system as effectively consisting of an infinitely large domain comprised of an infinite number of such sub-systems with the average temperature (salinity) gradient fixed to the values of $\Delta\Theta/L$ ($\Delta S/L$). Since the mean scalar gradient is everywhere the same, the unbounded gradient model is a suitable basis for analysis of equilibrium properties of salt-fingering fields. However, the special boundary condition (2.3) is somewhat artificial since it prevents the average background gradient from being influenced by the fluxes. This effect, on the other hand, can be clearly captured in the interface model that we proceed to discuss in what follows.

Although there are a variety of different possible definitions for the interface model, for present purposes, we choose to assume hyperbolic tangent forms for the initial conditions

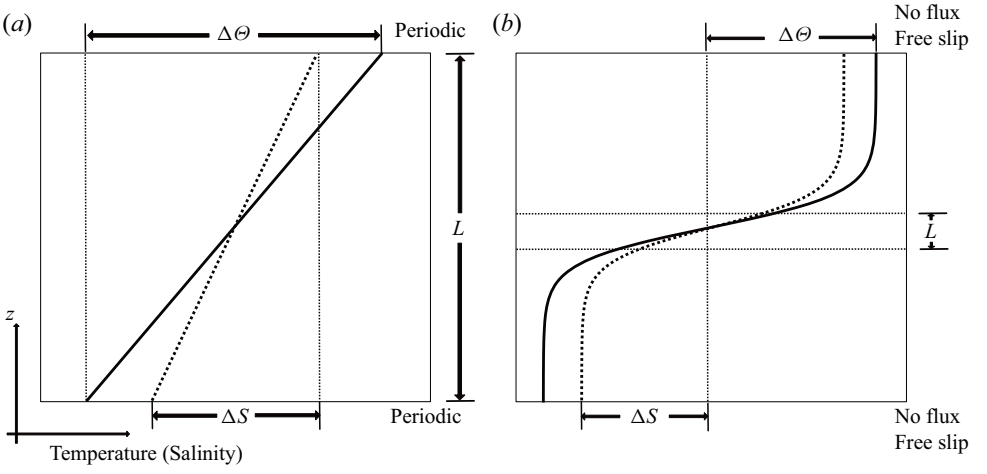

Figure 1. Illustration of the settings for the unbounded gradient model (*a*) and the interface model (*b*). In both parts of the figure, we use a solid line to represent the initial profile for temperature and the dashed line to represent the initial profile for salinity. Here $\Delta\Theta$, ΔS and L are the characteristic scales for potential temperature and salinity and length for each model that are used to non-dimensionalize each system.

for both temperature and salinity fields as in figure 1(*b*), namely:

$$\Theta(x, y, z) = \Delta\Theta \tanh\left(\frac{z}{L}\right), \tag{2.4a}$$

$$S(x, y, z) = \Delta S \tanh\left(\frac{z}{L}\right). \tag{2.4b}$$

In the formulation of this model we also assume periodic boundary conditions in the horizontal coordinates for both of the scalar fields (Θ, S) and velocity vector field $\boldsymbol{u}$. In the vertical coordinate direction we will assume free-slip, no-flux boundary conditions for both top and bottom boundaries of the domain.

In figure 1 we have also shown the length scale L, temperature scale $\Delta\Theta$ and salinity scale ΔS that we will use to non-dimensionalize the field equations describing this system: in the unbounded gradient model, $\Delta\Theta$ and ΔS are the corresponding scalar variations across the domain and L is the vertical height of the domain; whereas in the interface model, $\Delta\Theta$ and ΔS are half the variations of the temperature and salinity fields across the interface and L is the measure of interface depth so that $\Delta\Theta/L(\Delta S/L)$ represent the temperature/salinity gradients at the midpoint of the interface.

The original Boussinesq equations (2.1) with the incompressibility condition (2.1*d*) can then be non-dimensionalized assuming length scale L, time scale L^2/κ_θ and scalar scales $\Delta\Theta$, ΔS to obtain

$$\frac{\mathrm{D}u_*}{\mathrm{D}t_*} = -\frac{\partial p_*}{\partial x_*} + Pr\nabla_*^2 u_*, \tag{2.5a}$$

$$\frac{\mathrm{D}v_*}{\mathrm{D}t_*} = -\frac{\partial p_*}{\partial y_*} + Pr\nabla_*^2 v_*, \tag{2.5b}$$

$$\frac{\mathrm{D}w_*}{\mathrm{D}t_*} = -\frac{\partial p_*}{\partial z_*} + RaPr\Theta_* - RaPrS_*/R_\rho + Pr\nabla_*^2 w_*, \tag{2.5c}$$

$$\nabla_* \cdot \boldsymbol{u}_* = 0, \tag{2.5d}$$

Non-dimensional transformation	Non-dimensional number
$\boldsymbol{u}_* = (L/\kappa_\theta)\boldsymbol{u}$	$Pr = \nu/\kappa_\theta$: Prandtl number
$\partial/\partial x_* = L\partial/\partial x$	$Ra = g\alpha\Delta\Theta L^3/\nu\kappa_\theta$: Thermal Rayleigh number
$\partial/\partial t_* = (L^2/\kappa_\theta)\partial/\partial t$	$\tau = \kappa_s/\kappa_\theta$: Diffusivity ratio
$\boldsymbol{\nabla}_* = L\boldsymbol{\nabla}$	$R_\rho = \alpha\Delta\Theta/\beta\Delta S$: (Bulk) Density ratio
$p_* = p'L^2/(\kappa_\theta^2\rho_0)$	
$\Theta_* = (\Theta - \Theta_0)/\Delta\Theta$	
$S_* = (S - S_0)/\Delta S$	
$F_{\Theta *} = F_\Theta L/(\kappa_\theta\Delta\Theta)$	
$F_{S*} = F_S L/(\kappa_\theta\Delta S)$	
$\mathcal{H}_{\Theta *} = \mathcal{H}_\Theta L/(\kappa_\theta\Delta\Theta\rho_0\alpha g)$	
$\mathcal{H}_{S*} = \mathcal{H}_S L/(\kappa_\theta\Delta S\rho_0\beta g)$	

Table 1. Non-dimensional transformation and definition of non-dimensional numbers.

$$\frac{\mathrm{D}\Theta_*}{\mathrm{D}t_*} = \nabla_*^2\Theta_*, \tag{2.5e}$$

$$\frac{\mathrm{D}S_*}{\mathrm{D}t_*} = \tau\nabla_*^2 S_*, \tag{2.5f}$$

in which we have employed asterisks to denote non-dimensional variables. The non-dimensional transformation for each variable as well as the definition of non-dimensional parameters that appear in this non-dimensional system are listed in table 1. The Prandtl number and the diffusivity ratio are fixed to typical oceanographic values ($Pr = 7$ and $\tau = 0.01$) in this paper. The thermal Rayleigh number is essentially controlling the size of the system relative to the scale of the finger width, so that the volume-averaged physical quantities of the system are insensitive to variation of Ra as long as Ra is high enough (no less than order 10^7 to guarantee that the system contains sufficient fingers so that horizontal averages are meaningful). The dominant non-dimensional number of the system is then the bulk density ratio R_ρ, which measures the degree of compensation between temperature and salinity gradients in terms of their effects on density stratification. The system will be susceptible to salt-fingering instability when R_ρ satisfies $1 < R_\rho < 1/\tau$ (for both models), as revealed by linear stability analysis (e.g. Walin 1964; Baines & Gill 1969). The values of Ra and R_ρ employed in our numerical simulations for both the unbounded gradient model and the interface model will be discussed in detail in § 3 of this paper.

2.2. *Energy budget equations and irreversible fluxes*

In a salt-fingering-favourable system the unstably stratified salinity field releases its associated potential energy to create the kinetic energy required for mixing. This leads to an 'up-gradient' density flux that might be seen as somewhat counterintuitive. In this subsection we will discuss the energy budgets in the salt-fingering system from a somewhat novel perspective that separates the potential energy into a linear combination of those associated with temperature and salinity separately (this can also be applied to the diffusive convection counterpart to the salt-fingering system that we will discuss elsewhere). Application of this methodology will enable us to discuss the 'true' irreversible mixing in each of these two fields.

We begin by defining the average potential energy PE of the system in a certain volume V as

$$PE = \langle \rho g z \rangle = \frac{1}{V} \int \rho g z \, \mathrm{d}V, \tag{2.6}$$

where $\langle \cdot \rangle$ represents volume averages over the system of interest.

Due to our assumption of a linear equation of state (2.1g), we may further decompose the potential energy PE into a temperature component PE_Θ and a salinity component PE_S as

$$PE = \langle \rho g z \rangle, \tag{2.7a}$$
$$= \langle \rho_0 g z \rangle - \langle \rho_0 \alpha (\Theta - \Theta_0) g z \rangle + \langle \rho_0 \beta (S - S_0) g z \rangle, \tag{2.7b}$$
$$= \langle (1 + \alpha \Theta_0 - \beta S_0) \rho_0 g z \rangle - \rho_0 \alpha g \langle \Theta z \rangle + \rho_0 \beta g \langle S z \rangle, \tag{2.7c}$$
$$\equiv PE_0 + PE_\Theta + PE_S, \tag{2.7d}$$

where PE_Θ and PE_S denote the potential energy contributed by the temperature and salinity stratification of the fluid, separately. Equation (2.7) shows that the total potential energy can be viewed as a simple linear combination of PE_Θ and PE_S, a result that depends only upon the assumption of a linear equation of state. Here PE_0 is just a constant that may be ignored as it can play no role in the understanding of mixing processes.

The evolution of PE, PE_Θ, as well as PE_S in a closed system subject to the Boussinesq approximation satisfy the simple evolution equations

$$\frac{\mathrm{d}PE}{\mathrm{d}t} = \mathcal{D}_p + \mathcal{H}, \tag{2.8a}$$
$$\frac{\mathrm{d}PE_\Theta}{\mathrm{d}t} = \mathcal{D}_{p\Theta} + \mathcal{H}_\Theta, \tag{2.8b}$$
$$\frac{\mathrm{d}PE_S}{\mathrm{d}t} = \mathcal{D}_{pS} + \mathcal{H}_S, \tag{2.8c}$$

in which

$$\mathcal{H}_\Theta = -\rho_0 g \alpha \langle \Theta'(x, y, z, t) w'(x, y, z, t) \rangle, \tag{2.9a}$$
$$\mathcal{H}_S = \rho_0 g \beta \langle S'(x, y, z, t) w'(x, y, z, t) \rangle, \tag{2.9b}$$
$$\mathcal{H} = \mathcal{H}_\Theta + \mathcal{H}_S \tag{2.9c}$$
$$= g \langle \rho'(x, y, z, t) w'(x, y, z, t) \rangle, \tag{2.9d}$$
$$\mathcal{D}_{p\Theta} = \rho_0 g \alpha \kappa_\Theta \left\langle \frac{\partial \bar{\Theta}(z)}{\partial z} \right\rangle, \tag{2.9e}$$
$$\mathcal{D}_{pS} = -\rho_0 g \beta \kappa_S \left\langle \frac{\partial \bar{S}(z)}{\partial z} \right\rangle, \tag{2.9f}$$
$$\mathcal{D}_p = \mathcal{D}_{p\Theta} + \mathcal{D}_{pS}. \tag{2.9g}$$

In the above equations the overbar $\bar{f}(z)$ represents the horizontal average of field f and f' represents the deviation from it, i.e. $f'(x, y, z, t) = f(x, y, z, t) - \bar{f}(z)$. Here $\mathcal{H}$ represents the total buoyancy flux which is comprised of contributions from heat $\mathcal{H}_\Theta$ and salt $\mathcal{H}_S$; $\mathcal{D}_p$ represents the irreversible energy transfer associated with molecular diffusivity of both

diffusing species ($\mathcal{D}_{p\Theta}$ and $\mathcal{D}_{pS}$) in the motionless background that cannot be influenced by the turbulent motions.

In a system that supports salt-fingering instability, there is warm salty water lying above cold fresh water, leading upon the development of instability involving both heat flux $F_\Theta \equiv \langle w'\Theta' \rangle$ and salt flux $F_S \equiv \langle w'S' \rangle$ directed downwards, and, thus, $\mathcal{H}_\Theta > 0, \mathcal{H}_S < 0$ from ((2.9*b*), (2.9*c*)). Meanwhile, positive vertical gradients for both Θ and S will lead to $\mathcal{D}_{p\Theta} > 0$ and $\mathcal{D}_{pS} < 0$. This suggests a continuously increasing temperature potential energy $\mathrm{d}PE_\Theta/\mathrm{d}t > 0$ as well as a continuously decreasing salinity potential energy $\mathrm{d}PE_S/\mathrm{d}t < 0$ (from (2.8*b*) and (2.8*c*)), which implies that the salinity field is releasing potential energy whereas the temperature field is gaining potential energy in the salt-fingering field. The ratio of these buoyancy fluxes ($\gamma = |\mathcal{H}_\Theta|/|\mathcal{H}_S| = \alpha\langle w'\Theta' \rangle/\beta\langle w'S' \rangle$) is always smaller than 1 due to more effective salt exchange than heat exchange in the fingering system (Radko 2013). This fact ensures that $\mathcal{H} = \mathcal{H}_\Theta + \mathcal{H}_S < 0$ and, thus, the system is continuously releasing potential energy. These fluxes, following the initial onset of instability, eventually impact the average kinetic energy of the system which is defined as $KE \equiv \langle 1/2\rho_0 \boldsymbol{u}^2 \rangle$, whose evolution in a closed system can be shown to be

$$\frac{\mathrm{d}KE}{\mathrm{d}t} = -\mathcal{H} - \epsilon, \tag{2.10}$$

in which the viscous dissipation ϵ is $2\rho_o \nu \langle e_{ij} e_{ij} \rangle$. These two terms, which are of opposite sign, balance each other in an equilibrium (statistical equilibrium) state of the system.

The above definitions for heat and salt derived buoyancy flux ($\mathcal{H}_\Theta$, $\mathcal{H}_S$) and flux ratio γ are the quantities that have been employed in the discussion of double diffusion processes (see, e.g. Shen 1995; Traxler *et al.* 2011; Radko & Smith 2012). However, these definitions clearly fail to distinguish the differences between reversible stirring and irreversible mixing, both of which will be contributing to the transfer of energy between *PE* and *KE*. As in the shear-driven stratified turbulence case (see Winters *et al.* 1995; Caulfield & Peltier 2000; Peltier & Caulfield 2003), stirring refers to the temporary exchange between *PE* and *KE* caused by large-scale fluid motion which is reversible in principle and cannot contribute to irreversible mixing which occurs at the molecular scale. The critical step in the recognition of whether irreversible mixing occurs is to monitor whether the background potential energy is evolving as the turbulence continues. As illustrated in figure 2 of Caulfield & Peltier (2000) and figure 2 of Peltier & Caulfield (2003), the background potential energy (also known as the minimum potential energy) is the potential energy that would be associated with the adiabatic redistribution of fluid parcels in such a way that the density $\rho(x, y, z, t)$ is monotonically decreasing with height and, therefore, statically stable. The definition of the background potential energy guarantees that it will not be influenced by the macroscopic fluid motions (the stirring processes), rather, the sorted fluid elements will only lead to an increase of background potential energy in time when molecular diffusion is irreversibly changing the densities of neighbouring fluid parcels.

In our analysis of the salt-fingering system we will employ similar ideas to distinguish between irreversible mixing and reversible stirring. However, as density is influenced by both temperature and salinity in salt-fingering convection, we will need to sort both scalar fields separately rather than sorting the density field. Otherwise, the temperature and salinity information would be lost in the sorting process and it would then be impossible to determine distinct heat and salinity fluxes. How this sorting procedure should be performed will depend strongly upon the particular flavour of doubly diffusive turbulence being analysed: in the salt-fingering problem, since the salinity field is unstably stratified

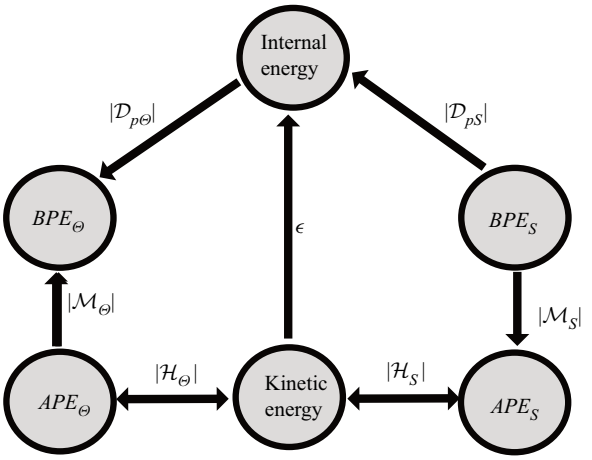

Figure 2. Exchange of energy fluxes between different energy reservoirs, graphics for (2.10), (2.12) and (2.13).

which supplies energy to both the potential energy associated with the temperature field and the kinetic energy reservoir, we need to adiabatically rearrange the salinity profile into a state such that the salinity is monotonically increasing with height (corresponding to a top heavy structure). In this way, irreversible mixing in the salinity field will lead to a monotonic decrease of the background salinity related potential energy, which is consistent with the basic energy flows in the salt-fingering field. For the temperature field, this must also be adiabatically rearranged to a state in which temperature is monotonically increasing with height. (The sorting directions will be just opposite for both the temperature and the salinity field in a diffusive convection system, which we will address elsewhere.) Since temperature is negatively correlated with density, we essentially sort the temperature to a bottom heavy structure just as in the shear-driven turbulence case. Irreversible mixing of the temperature field will lead to an increase in the corresponding background temperature potential energy, which is then also consistent with the direction of the energy flow in the salt-fingering problem.

Explicitly, we firstly rearrange all the fluid elements adiabatically to a configuration in which warmer elements are always on top of the colder elements. In this way the temperature of the sorted configuration will only depend on the vertical coordinate, which can be denoted as $\Theta_\star(z, t)$. Then we do the sorting of the salinity field to ensure that the saltier elements are always above the fresher elements, which will give us a sorted salinity configuration $S_\star(z, t)$.

The background potential energy for temperature BPE_Θ and the background potential energy for salinity BPE_S can then be defined based on these two profiles as

$$BPE_\Theta = -\rho_0 \alpha g \langle \Theta_\star(z) z \rangle, \tag{2.11a}$$

$$BPE_S = \rho_0 \beta g \langle S_\star(z) z \rangle, \tag{2.11b}$$

$$BPE = BPE_\Theta + BPE_S. \tag{2.11c}$$

In all the possible rearrangements of the fluid elements, $\Theta_\star(z)$ is the configuration which has the minimum PE_Θ of all the configurations (thus, $BPE_\Theta \leq PE_\Theta$), and $S_\star(z)$ is the configuration which has the maximum PE_S of all the configurations (thus, $BPE_S \geq PE_S$). As the temperature diffusion term $\kappa_\theta \nabla^2 \Theta$ in (2.1*e*) mixes the warmer water columns with the colder water columns, the total mass of the sorted profile $\Theta_\star(z)$ stays the same (in

a closed system) but the centre of gravity is lifted, leading to the increase of BPE_Θ. Meanwhile, macroscopic fluid motion (stirring) only changes the relative positions of fluid parcels, which will not influence the configurations after sorting and, thus, will not lead to changes of BPE_Θ. Thus, the rate of change of BPE_Θ will reflect the strength of irreversible mixing in the temperature field. The same analysis applies for the salinity field.

The above analysis can be justified simply by investigation of the evolution equations of BPE_Θ and BPE_S. Winters *et al.* (1995) derived the evolution equation for the background potential energy in the shear-driven case, which can be directly applied to the evolution for BPE_Θ and BPE_S in the double diffusion case of interest to us here since both temperature and salinity are governed by the same advection–diffusion equations as that which governs density in the shear-driven stratified turbulence case discussed in Winters *et al.* (1995). In a closed system, these evolution equations can be shown to be

$$\frac{\mathrm{d}}{\mathrm{d}t}BPE_\Theta = \mathcal{M}_\Theta + D_{p\Theta}, \tag{2.12a}$$

$$\frac{\mathrm{d}}{\mathrm{d}t}BPE_S = \mathcal{M}_S + D_{pS}, \tag{2.12b}$$

$$\mathcal{M}_\Theta + \mathcal{D}_{p\Theta} = \kappa_\theta \rho_0 \alpha g \left\langle \frac{\mathrm{d}z_{\theta\star}}{\mathrm{d}\Theta} |\nabla\Theta|^2 \right\rangle, \tag{2.12c}$$

$$\mathcal{M}_S + \mathcal{D}_{pS} = -\kappa_s \rho_0 \beta g \left\langle \frac{\mathrm{d}z_{s\star}}{\mathrm{d}S} |\nabla S|^2 \right\rangle. \tag{2.12d}$$

Since both temperature and salinity profiles are sorted to increase upwards, it is clear that $\mathcal{M}_\Theta + \mathcal{D}_{p\Theta} > 0$ and $\mathcal{M}_S + \mathcal{D}_{pS} < 0$ from ((2.12*c*) and (2.12*d*)). Thus, we have confirmed our analysis above that BPE_Θ will always be a monotonically increasing function with time while BPE_S will be a monotonically decreasing function with time. The distinctions between $\mathcal{M}_\Theta(\mathcal{M}_S)$ and $D_{p\Theta}$ (D_{pS}) were introduced in Caulfield & Peltier (2000) and Peltier & Caulfield (2003), in which $D_{p\Theta}$ (D_{pS}) characterizes energy transfer in the motionless background, and $\mathcal{M}_\Theta(\mathcal{M}_S)$ represents the part of the irreversible fluxes induced by motion which produces a much larger iso-scalar surface area for mixing to occur.

Distinct available potential energies may then be defined as the difference between the potential energies and background potential energies, namely:

$$APE_\Theta = PE_\Theta - BPE_\Theta, \tag{2.13a}$$

$$APE_S = PE_S - BPE_S, \tag{2.13b}$$

$$\frac{\mathrm{d}}{\mathrm{d}t}APE_\Theta = \mathcal{H}_\Theta - \mathcal{M}_\Theta, \tag{2.13c}$$

$$\frac{\mathrm{d}}{\mathrm{d}t}APE_S = \mathcal{H}_S - \mathcal{M}_S. \tag{2.13d}$$

Analysing the energy flows in the available potential energy reservoirs will lead to a qualitatively useful depiction of energy flows between the different energy reservoirs that are active in salt-fingering turbulence, as illustrated in figure 2. Concerning the temperature field, energy is being transferred from the *KE* reservoir into the PE_Θ reservoir at a rate represented by $\mathcal{H}_\Theta$. A portion of the energy flux is effected through irreversible processes (mixing) $\mathcal{M}_\Theta$ and this is eventually transferred into the background potential

energy BPE_Θ, while the remaining portion of this energy flux $\mathcal{H}_\Theta - \mathcal{M}_\Theta$ enters into the APE_Θ reservoir. The energies stored in APE_Θ is 'available', meaning that it may be released back to the KE reservoir through a negative flux $\mathcal{H}_\Theta$. On the other hand, for the salinity field, energy is transferred from the PE_S reservoir into the KE reservoir. The irreversible flux $\mathcal{M}_S$ transports energy from background potential energy BPE_S to the APE_S irreversibly, which leads to the monotonic decrease of BPE_S. This loss of the energy in APE_S to KE, on the other hand, is reversible and can potentially be returned back to APE_S through a positive $\mathcal{H}_S$.

2.3. *Evaluating irreversible salt-fingering fluxes in two different models*

We will first discuss the application of the above formalism to the interface model. As the interface model is strongly inhomogeneous in the vertical direction, it is expected to be useful to investigate the variation of the irreversible fluxes of heat and salt in the vertical direction across the finite depth of the interface. The depth-dependent irreversible heat and salt fluxes are defined as

$$F_\Theta^{irr}(z_{\theta\star}) = -\kappa_\theta \frac{\mathrm{d}z_{\theta\star}}{\mathrm{d}\Theta} \overline{|\nabla\Theta'(x,y,z)|^2}_{z_{\theta\star}}, \tag{2.14a}$$

$$F_S^{irr}(z_{s\star}) = -\kappa_s \frac{\mathrm{d}z_{s\star}}{\mathrm{d}S} \overline{|\nabla S'(x,y,z)|^2}_{z_{s\star}}, \tag{2.14b}$$

in which the irreversible fluxes have depth-dependence on the sorted coordinate $z_{\theta\star}$ ($z_{s\star}$) and the representation $|f(x,y,z)|_{z_{\theta\star}(z_{s\star})}$ refers to the average of the field $f(x,y,z)$ with the same $z_{\theta\star}(z_{s\star})$. Such depth-dependent definitions are consistent with the bulk-averaged definitions (2.12) (as discussed in Salehipour & Peltier (2015)). Although the above definitions of irreversible heat flux (salt flux) are closely related to the previously mentioned heat (salt)-induced buoyancy flux through $\mathcal{M}_\Theta(z_{\theta\star}) = -g\alpha F_\Theta^{irr}(z_{\theta\star})$ ($\mathcal{M}_S(z_{s\star}) = g\beta F_S^{irr}(z_{s\star})$), we prefer to use these more straightforward quantities of $F_\Theta^{irr}(z_{\theta\star})$ and $F_S^{irr}(z_{\theta\star})$ to be compared with $F_\Theta(z)$ and $F_s(z)$ in what follows.

The calculation of irreversible fluxes in the unbounded gradient model, on the other hand, is not nearly so straightforward. As we have discussed in § 2.1, the unbounded gradient model essentially describes an infinitely large, homogeneous system that is defined by applying the periodic boundary conditions in all three coordinate directions. It is for this reason that we have to consider fluid elements that are not 'directly' contained in the simulation domain when the time-dependent adiabatic rearrangements of fluid parcels are constructed. Consider the typical iso-temperature contour (non-dimensionalized) in the sketch shown in figure 3(*a*), the periodic vertical boundary condition applied allows for the occurrence of the intersections of the iso-temperature contour with the top and bottom boundaries. If we sort the fluid elements only in the simulation domain, we would obtain the result shown in figure 3(*b*), i.e. the sorted profiles will have a larger vertical gradient near the vertical boundaries, which is pathological since the artifacts near the vertical boundaries have been artificially introduced. Thus, we sort the fluid elements in the new domain shown in figure 3(*c*) which contains essentially the same fluid elements as the original domain and retains the same boundary conditions (repeatable vertically) as before. Sorting in this newly defined domain precisely avoids the inhomogeneous-gradient problem illustrated in figure 3(*b*) and is applied to correctly sort the fluid parcels involved in the salt-fingering turbulent flows to be discussed in what follows.

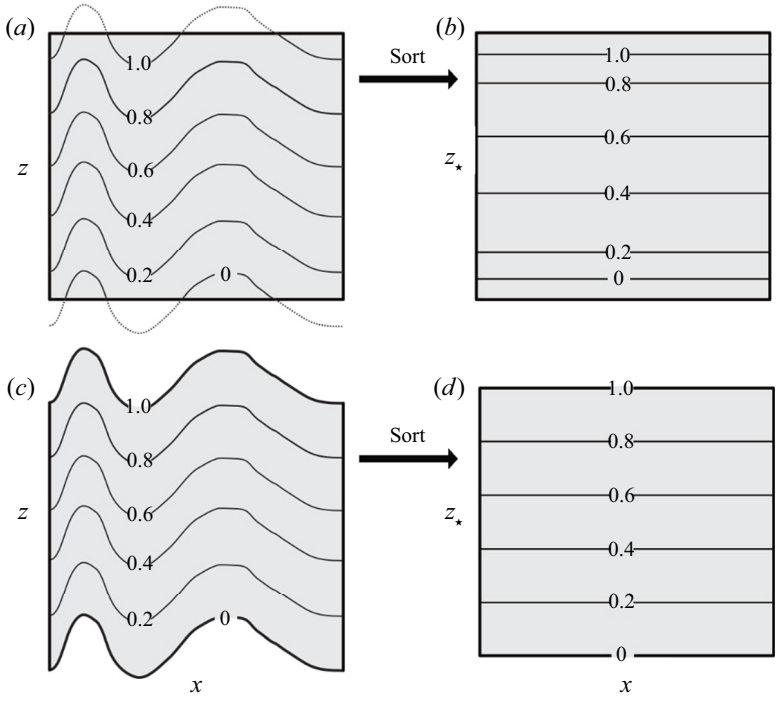

Figure 3. Illustration of the incorrect method of sorting fluid elements (*a*,*b*) and the correct method of fluid-element sorting (*c*,*d*) to calculate irreversible fluxes in the unbounded gradient model. Panels (*a*) and (*c*) illustrate a typical iso-temperature contour (or surface in three dimensions) in the unbounded gradient model, (*b*) shows the sorted temperature when the sort region is depicted by the thick line in (*a*), while (*d*) shows the sorted temperature when the sort region is depicted by the thick line in (*c*).

2.4. *An alternative definition of background potential energies in double-diffusive systems*

In this subsection we will discuss an alternative possibility for extending the idea of background potential energy from a single-component system to a doubly diffusive system. This approach has been discussed in detail in the recent work of Middleton & Taylor (2020) and we will present and discuss their main results using our notation in this subsection. These results will then be compared with our results presented in the previous subsection in (2.12)–(2.14), on the basis of which we will argue that the definitions of background potential energies proposed in the current paper are distinctly preferable for application to the study of irreversible mixing in doubly diffusive systems.

As we have discussed above, the background potential energy in a single-component system is associated with the stable rearrangement of the fluid parcels based on their densities. Middleton & Taylor (2020) directly extends this definition of background potential energy to the double-diffusive system, as

$$BPE^{MT} = g\langle \rho z_{\rho\star} \rangle, \tag{2.15}$$

where $z_{\rho\star}(x, y, z, t)$ represents the vertical position in the sorted profile of the fluid parcel at (x, y, z, t) and $\rho(x, y, z, t)$ is determined by the temperature and salinity through the linear equation of state (2.1*g*). In a closed system the evolution of BPE^{MT} can be derived

following the same strategy as in Winters *et al.* (1995) to be

$$\frac{\mathrm{d}}{\mathrm{d}t}BPE^{MT} = -\kappa_\theta g\left\langle \frac{\mathrm{d}z_{\rho\star}}{\mathrm{d}\rho}|\nabla\rho_\theta|^2\right\rangle - \kappa_s g\left\langle \frac{\mathrm{d}z_{\rho\star}}{\mathrm{d}\rho}|\nabla\rho_s|^2\right\rangle - (\kappa_\theta+\kappa_s)g\left\langle \frac{\mathrm{d}z_{\rho\star}}{\mathrm{d}\rho}(\nabla\rho_s\cdot\nabla\rho_\theta)\right\rangle, \tag{2.16}$$

where $\rho_\theta \equiv -\rho_0\alpha(\Theta-\Theta_0)$ and $\rho_s \equiv \rho_0\beta(S-S_0)$ are the components of density that are determined by the temperature field and salinity field separately. Equation (2.16) is essentially equivalent to equation (2.19) of Middleton & Taylor (2020) in a closed system. In order to make a clearer comparison, we rewrite the evolution equation for the background potential energies (2.12*c*) using ρ_θ and ρ_S as

$$\frac{\mathrm{d}}{\mathrm{d}t}BPE = \frac{\mathrm{d}}{\mathrm{d}t}BPE_\Theta + \frac{\mathrm{d}}{\mathrm{d}t}BPE_S = -\kappa_\theta g\left\langle \frac{\mathrm{d}z_{\theta\star}}{\mathrm{d}\rho_\theta}|\nabla\rho_\theta|^2\right\rangle - \kappa_s g\left\langle \frac{\mathrm{d}z_{s\star}}{\mathrm{d}\rho_s}|\nabla\rho_s|^2\right\rangle. \tag{2.17}$$

The first two terms on the right-hand side of (2.16) have very similar forms to those describing our irreversible buoyancy fluxes defined in (2.17). In fact, there are only two differences between these two forms: firstly, the derivatives of the sorted vertical coordinate are computed with respect to different scalars in (2.16) and (2.17); secondly, the two terms in (2.16) are both positive, while in (2.17) the temperature term is positive whereas the salinity term is negative (in a salt-fingering-favourable configuration). Both of these distinctions are suggesting that the terms in (2.16) cannot be regarded as representations of irreversible mixing processes. Firstly, the appearance of total density ρ in the first two terms of (2.16) renders them not independent: different salinity configurations will change the value of the temperature term and vice versa. However, the salinity dissipation process is clearly independent of the heat dissipation process, making the correlations in (2.16) difficult to interpret. Secondly, salinity mixing in a salt-fingering-favourable environment mixes the upper layer salty water with lower layer fresh water, which would lead to a decrease rather than increase in potential energy. This further fact makes it difficult to interpret the second term in (2.16) as representing salinity mixing.

The third term in (2.16) is negative in a salt-fingering-favourable environment, since thermal and saline density components compensate each other to make $\nabla\rho_\theta\cdot\nabla\rho_s<0$. The magnitude of this negative term can be larger than the first two positive terms in double-diffusive fields (as discussed in Middleton & Taylor (2020)), allowing BPE^{MT} to be released even in a closed system. This property contradicts the original physical meaning of the background potential energy that was defined in a single-component system, which can only increase in a closed system due to irreversible mixing processes. Our methodology described in §§ 2.2 and 2.3, on the other hand, perfectly retains the original physical meaning of background potential energies and provides intuitively reasonable forms for the irreversible fluxes in double-diffusive fields. It therefore seems clear that the formalism we have developed for the separation of irreversible and reversible fluxes in doubly diffusive convection is to be preferred. The price to be paid for its use is that at each timestep in the evolution of the DNS, two full sorts of the individual fluid parcels must be performed. Since the algorithm we employ to perform the required sorts is highly parallelizable (as will be discussed in the next section), however, this fact is not an impediment to the use of this more accurate methodology.

3. Design of the direct numerical simulations and the numerical methodology employed

High-resolution DNS of salt-fingering turbulence simulations are performed for both the unbounded gradient model and the interface model, by solving the non-dimensional governing equations with the appropriate boundary and initial conditions for each model. We will choose the ratio of diffusivities to be $\tau = 0.01$ and the Prandtl number $Pr = 7$ in these simulations so as to mimic realistic oceanographic conditions.

For the purpose of the simulations to be performed using the unbounded gradient model, we will compile results for a range of, mostly equally spaced, values of R_ρ between 1 and 10 in order to explore a more extensive parameter space than in Radko & Smith (2012). The critical information for these 10 simulations using the unbounded gradient model is listed in table 2 with simulation numbers from 1 to 10. Linear stability analyses have been performed as a basis on which to determine the horizontal width of the fastest growing mode of salt fingering at each of these different values of R_ρ, and these widths are always at the typical length scale of the salt-fingering problem for which $d = (\kappa_\theta \nu/(g\alpha\Theta_z))^{1/4}$ (see Radko 2013) and are summarized in table 2. The Rayleigh number of the simulation can then be determined for each simulation by recognizing the relationship $Ra = (L/d)^4$. For the unbounded gradient model, the simulation domain will be taken to include 5 *FGW* (*FGW* is the horizontal width of the fastest growing mode predicted by linear stability analysis which has the scale of d) in both horizontal directions and 10 *FGW* in the vertical direction. The choices of size and aspect ratio for the simulation domain have been previously established for analyses of turbulence in the unbounded gradient model (see a detailed discussion in the appendix of Traxler *et al.* (2011)). A resolution of $385 \times 385 \times 770$ grid points is employed for simulations with $1 < R_\rho < 8$ and a slightly coarser resolution of $266 \times 266 \times 532$ grid points is employed with $R_\rho = 8, 9$ and 10. Although the resolved scale may be more than an order of magnitude larger than the Batchelor scale (Batchelor 1959) at which salinity fluctuations are dissipated, it can be shown to be sufficient to study the equilibrium fluxes in the unbounded gradient model (as discussed in appendix A). A small amplitude seed of the form of $\lambda_{(\Theta,S,w)} \cos(k_{m*}x) \cos(k_{m*}y)$ (here $k_{m*} = 2\pi L/FGW$ is the non-dimensional fastest growing wavenumber predicted by the linear stability analysis, $(\lambda_\Theta, \lambda_S, \lambda_w)$ are proportional to the eigenfunction of the fastest growing mode in linear stability analysis and the amplitude of the salinity mode λ_S is set to $0.001\Delta S$) is super-imposed on the initial background profile, together with random noise whose amplitude is 1000 times smaller than either $\Delta\Theta$ or ΔS to provide the perturbation needed for the development of secondary zig-zag instability as discussed in what follows.

The additional simulations to be discussed concern the study of the interface model also at $\tau = 0.01$ and $Pr = 7$ for three different values of R_ρ. The corresponding information is listed under simulation numbers 11, 12 and 13 in table 2 as in the unbounded gradient model case. For the analysis of results for this model, we have been working in a much larger domain (30 *FGW* $\times$ 5 *FGW* $\times$ 100 *FGW*) in order to study the detailed local behaviour of the system. A corresponding much higher resolution is thus needed for simulations in the interface model. Because the most intense mixing usually occurs within the central region of the domain, we can generally reduce the box resolution near the boundaries. In order to investigate the utility of this numerical design we performed test runs to determine the Batchelor scale as a function of depth, on the basis of which we have designed the most efficient depth-dependent resolution of the box needed to resolve the salinity Batchelor scale at each depth. The details of how the resolution is determined can be found in the appendix A.

Numbering	Models	R_ρ	FGW	Ra	Resolution
1	Unbounded	1.1	$10.2d$	1.10×10^8	$385 \times 385 \times 770$
2	Unbounded	2	$7.54d$	3.23×10^7	$385 \times 385 \times 770$
3	Unbounded	3	$7.11d$	2.56×10^7	$385 \times 385 \times 770$
4	Unbounded	4	$6.98d$	2.38×10^7	$385 \times 385 \times 770$
5	Unbounded	5	$6.93d$	2.31×10^7	$385 \times 385 \times 770$
6	Unbounded	6	$6.93d$	2.30×10^7	$385 \times 385 \times 770$
7	Unbounded	7	$6.94d$	2.32×10^7	$385 \times 385 \times 770$
8	Unbounded	8	$6.96d$	2.34×10^7	$266 \times 266 \times 532$
9	Unbounded	9	$6.98d$	2.38×10^7	$266 \times 266 \times 532$
10	Unbounded	10	$7.01d$	2.42×10^7	$266 \times 266 \times 532$
11	Interface	2	$7.86d$	3.82×10^7	$1582 \times 266 \times 4424$
12	Interface	5	$7.27d$	2.80×10^7	$1085 \times 182 \times 3143$
13	Interface	8	$7.31d$	2.85×10^7	$952 \times 161 \times 2716$

Table 2. Summary of the numerical settings for 13 simulations performed in both the unbounded gradient system and the interface system.

All of our simulations are performed using the open-source computational fluid dynamics software package Nek5000, developed by Argonne National Laboratory (Fischer *et al.* 2008). The software package Nek5000 is based on the spectral element method (Fischer, Kruse & Loth 2002), discretized using Nth order Lagrange polynomial interpolants following the $P_N - P_{N-2}$ formulation of Maday, Patera & Rønquist (1990). This methodology was initially designed to deal with transitional and turbulent flows in complex geometries (Fischer *et al.* 2002) and was later found to be a powerful tool for the simulation of high-Reynolds-number shear-induced stratified turbulence flows (see Salehipour & Peltier 2015; Salehipour, Caulfield & Peltier 2016). In the post-processing stage a parallel sorting algorithm (rather than serial sorting algorithm) must be applied for the analysis in such high-resolution simulations for both time and memory considerations. Such an algorithm has already been designed and illustrated in detail in Salehipour & Peltier (2015), which will be applied in sorting both the temperature and salinity fields required in the current context.

4. DNS results

In this section we will first compare the strength of irreversible fluxes to traditionally defined fluxes in the unbounded gradient model in §§ 4.1.1 and 4.1.2. These comparisons will be presented as a function of stage in the evolution of the salt-fingering field in order to develop an understanding of the mechanisms involved in the determination of irreversible mixing. We will then describe a functional fit to the equilibrium fluxes of the unbounded gradient model in § 4.1.3. In § 4.2 the simulation results obtained for the interface model will be briefly described followed by a comparison of irreversible fluxes with traditionally defined fluxes as a function of depth. Finally, in § 4.2.3 we will compare the functional fit of § 4.1.3 with fluxes from the interface model. These comparisons will reveal a profoundly interesting relationship between the unbounded gradient model and the interface model. It must be recognized that the DNS results in this section will be presented in non-dimensional units, the definition of which has been listed in table 1 above.

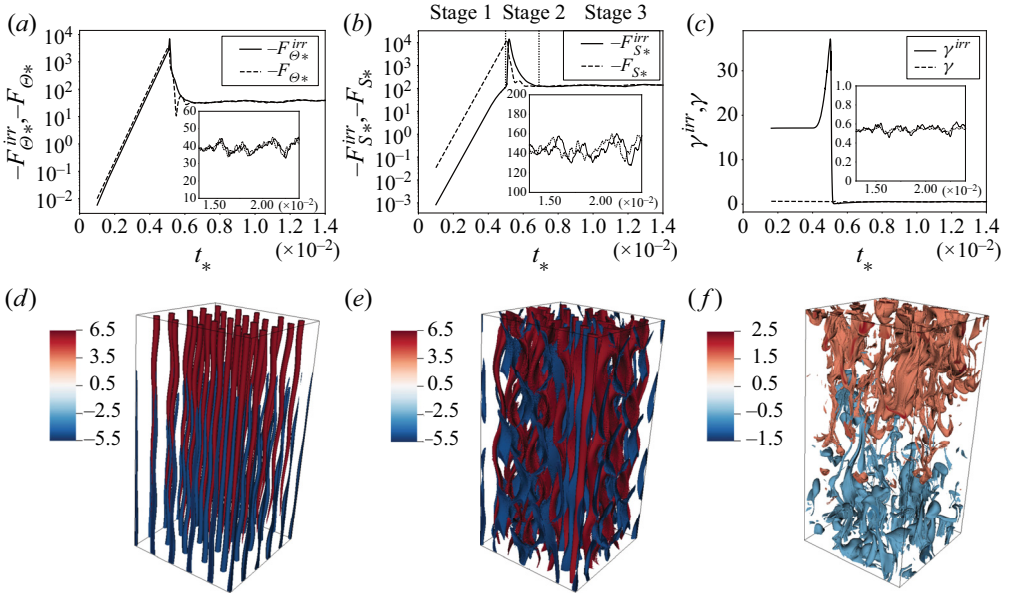

Figure 4. Evolution of non-dimensional heat diffusivities (*a*) and salt diffusivities (*b*) as well as flux ratio (*c*) in a DNS with $R_\rho = 2$, both traditional fluxes (or flux ratio) and irreversible fluxes (or flux ratio) are shown in dashed and solid lines, separately. Salinity fields are shown in (*d*)–(*f*) at non-dimensional times 0.00507, 0.00512, 0.00766 separately to illustrate the twisting of salt fingers under the action of the secondary zig-zag instabilities.

4.1. *Direct numerical simulation results for the unbounded gradient model*

4.1.1. *Stages of time-dependent evolution*

The evolution of salt fingers in the unbounded gradient model has been thoroughly studied and is well understood (e.g. Shen 1995; Traxler *et al.* 2011). There are generally three stages in this evolutionary process, which can be separated on the basis of the evolution of volume averaged traditionally defined fluxes $F_\Theta \equiv \langle w'\Theta' \rangle$, $F_S \equiv \langle w'S' \rangle$, an example of which is shown in the dashed curves in figure 4(*a*,*b*). In the first stage, the fastest growing mode of linear salt-fingering instability experiences exponential growth, which leads to the exponential growth of both vertical heat and salt fluxes as shown in figure 4(*a*,*b*). In the second stage, these very large vertical fluxes are eventually suppressed by the development of secondary zig-zag instabilities (as originally discussed by Holyer (1984)). This zig-zag instability introduces vertical shear of horizontal velocity which acts so as to introduce local tilt along the axis of the original long and slender salt fingers (the first slightly tilted fingers can be seen in figure 4*d*) and acts so as to break the individual fingers into patches (figure 4*e*). Following this zig-zag instability induced breakup of the initial fingers, the system then evolves into the third stage of activity in which the turbulent fields of both temperature and salinity have been statistically homogenized as depicted in figure 4(*f*).

4.1.2. *Results for the irreversible fluxes*

As discussed in § 2.2, only the irreversible component of the vertical fluxes may contribute to true mixing in the salt-fingering system and, therefore, to the eddy diffusivity which would be employed in a large-scale model that was unable to resolve the turbulence directly. These fluxes can be calculated in our DNS in the unbounded gradient model following the procedures discussed in § 2.3. The typical evolution of both the irreversible

heat flux F_Θ^{irr} and the irreversible salt flux F_S^{irr} are shown in the solid lines in figures 4(*a*) and 4(*b*) separately. Here F_Θ^{irr} follows almost the same trajectory as that for its traditionally defined counterpart F_Θ: F_Θ^{irr} experiences exponential growth in the initial phase of salt finger development, but decreases in strength once the zig-zag instability begins to twist the fingers and eventually equilibrates to very nearly the same value as the equilibrium F_Θ. However, the evolution of F_S^{irr} differs distinctly from that of F_S. In the initial phase of finger growth, F_S^{irr} grows at nearly the same growth rate as F_S but at any particular time remains smaller by more than an order of magnitude. This initial stage is followed by an even faster rate of growth that begins when F_S begins to decline. Here F_S^{irr} ascends to its peak value and then evolves towards the statistical equilibrium strength characteristic of stage 3 in which it has nearly the same value as F_S.

The above evolutionary trajectory of the fluxes can be understood by recognizing the physical meaning of irreversible fluxes – they represent the flux contributed by diffusion acting on sufficiently small scales so as to modify the temperature/salinity of the turbulently displaced fluid parcels and their neighbours. The traditionally defined fluxes F_S and F_Θ, however, only capture the extent to which fluid displaced from the high temperature/salinity environment is inserted into the low temperature/salinity environment. The difference between the strengths of these differently defined fluxes are closely related to rates of molecular diffusion. In the limiting case in which it may be assumed that the tracer diffuses infinitely quickly (horizontally), any displacement of a fluid parcel from a region in which the background tracer field has a low value into a region in which the background tracer field has a higher value will inevitably lead to irreversible mixing at the small scales with the same strength. In this case there will therefore be no distinctions between different definitions of the fluxes. Relaxing this constraint of infinite diffusivity slightly will lead to the case of the temperature field illustrated above: although the absolute value of molecular temperature diffusivity is small (around 1.7×10^{-7} m^2 s^{-1}), it is not a small value in the micro-scale system we are studying considering that we have non-dimensionalized the system in such a way that $\kappa_{\theta *} = 1$ (shown in table 1). In this circumstance, any displaced fluid parcel that has a different temperature from that of its surroundings will take some time to mix temperatures locally. It is for this reason that a small phase delay can be observed in figure 4(*a*): F_Θ^{irr} follows almost the same trend as F_Θ, it simply evolves somewhat more slowly. In other words, the displaced fluid parcels are eventually mixed in temperature with their surroundings quite efficiently.

The molecular diffusivity for salinity, on the other hand, is much smaller than temperature diffusivity ($\kappa_s = 0.01\kappa_\theta$ under oceanographic conditions and for the current simulations which are tuned to that environment), which leads to a more complicated picture than that for temperature discussed above. Quantitative analysis can be performed by considering the previously discussed different stages of salt finger development (stage 1) illustrated in figure 4(*d*), the fluid parcels can travel a very great distance vertically through the surroundings with much higher/lower salinity while leaving its original salinity essentially unchanged due to the extremely small value of the salinity diffusivity. In this process, only vanishingly small irreversible mixing for the salinity field F_S^{irr} occurs even though F_S is large (both F_S^{irr} and F_S are exponentially growing). In stage 2, however, the zig-zag instability begins to twist the fingering structures and to advect fluid parcels with extreme salinities into closer contact with their neighbours. This forces these fluid parcels to exchange salinity with neighbouring parcels (as can be seen in figure 4*e*), therefore, the more fingering structures are twisted and destroyed, the

stronger the irreversible mixing will be. This explains why F_S^{irr} dramatically increases right at the time when the zig-zag instability begins to suppress fingering growth as shown in figure 4(*b*). This is one of the most fundamental conclusions of this paper: while the traditionally defined salt flux provides a useful diagnostic of the salt-fingering generation mechanism, the irreversible salt flux is capturing the extent to which fingers are being destroyed. The final statistical equilibrium stage of salt-fingering turbulence can best be understood as a state in which there exists a balance between finger generation and disruption (the nature of this balance is captured in the theoretical model of Radko & Smith (2012)) which suggests that the equilibrium state is obtained when the growth rate of first-order fingering instability is balanced with the growth rate of the zig-zag instability). As the growth rate of fingers being generated at a given time will determine the number of fingers that are available for disruption at a later time, there is an expected phase delay between F_S^{irr} and F_S demonstrated in the high-resolution inset of figure 4(*b*).

After comparing the evolution of irreversible heat and salt fluxes in the unbounded gradient model above, it is also informative to discuss their ratios: the ratio of irreversible fluxes is defined as

$$\gamma^{irr} \equiv \frac{|\mathcal{M}_\Theta|}{|\mathcal{M}_\mathcal{S}|} = \frac{|\alpha F_\Theta^{irr}|}{|\beta F_S^{irr}|}. \tag{4.1}$$

The evolution of γ^{irr} is compared with the traditional definition γ in figure 4(*c*). The traditional γ in the salt finger growth stage (around 0.584) is a slight overestimation of the value of γ in the equilibrium stage (around 0.546), a trend that has been discussed in detail in earlier work of Traxler *et al.* (2011). However, the ratio of irreversible fluxes γ^{irr} is extremely high in the early stage of evolution of the turbulent flow simply due to the much higher temperature diffusivity than salinity diffusivity. Following the transition stage 2, γ^{irr} equilibrates at a level that is nearly the same at equilibrium as that for γ. However, the variations about the equilibrium are significantly stronger than those characteristic of the traditional ratio γ, which suggests a larger error bar is necessary for characterization of the numerically determined irreversible flux ratio. This effect is not due to larger variations in F_Θ^{irr} (F_S^{irr}) than F_Θ (F_S) (since they are characterized by fluctuations of similar magnitude as shown in figure 4*a*,*b*), but is simply due to the phase delays mentioned above: while irreversible temperature flux remains in phase with the finger generation process at a given time, the irreversible salinity flux is more nearly in phase with the finger disruption mechanism at a given time. Thus, the value of the irreversible flux ratio at a given time actually involves the state of the system that existed at a significantly earlier time, and this inevitably leads to stronger variations with time of γ^{irr} about its equilibrium value.

4.1.3. *Equilibrium fluxes and a revised scheme for the parameterization of salt-fingering turbulence in global ocean models*

As discussed above, the salt-fingering turbulence in the unbounded gradient model eventually evolves into an equilibrium state which is statistically stable. This makes it possible for us to obtain useful estimates of the diapycnal diffusivities based on the measured fluxes. Specifically, the diapycnal diffusivities can be calculated by substituting the equilibrium fluxes and the constant background gradients into the definitions, for both

R_ρ	$K_\Theta^{irr}/\kappa_\theta$	K_S^{irr}/κ_θ	γ^{irr}	Averaged intervals of t_*
1.1	240 ± 35	394 ± 49	0.671 ± 0.110	0.0024–0.0034
2	39.18 ± 6.1	143.6 ± 16.7	0.546 ± 0.090	0.013–0.024
3	23.32 ± 5.2	131.1 ± 22.8	0.534 ± 0.090	0.015–0.043
4	12.59 ± 1.6	103.6 ± 16.3	0.488 ± 0.080	0.038–0.048
5	10.10 ± 1.0	104.7 ± 13.5	0.483 ± 0.077	0.037–0.054
6	6.78 ± 0.72	87.6 ± 8.57	0.471 ± 0.066	0.06–0.085
7	5.31 ± 0.46	82.0 ± 10.9	0.453 ± 0.055	0.050–0.094
8	4.47 ± 0.61	77.4 ± 13.8	0.464 ± 0.064	0.09–0.19
9	3.85 ± 0.62	75.5 ± 11.8	0.472 ± 0.074	0.07–0.24
10	3.45 ± 0.75	71.7 ± 15.0	0.482 ± 0.070	0.10–0.25

Table 3. Equilibrium K_Θ^{irr}, K_S^{irr}, as well as γ^{irr} averaged over the statistical equilibrium state of simulation numbers 1–10.

traditionally defined fluxes and the irreversible fluxes, as

$$K_\Theta = -\frac{F_\Theta}{\Theta_{z0}}, \tag{4.2a}$$

$$K_S = -\frac{F_S}{S_{z0}}, \tag{4.2b}$$

$$K_\Theta^{irr} = -\frac{F_\Theta^{irr}}{\Theta_{z0}}, \tag{4.2c}$$

$$K_S^{irr} = -\frac{F_S^{irr}}{S_{z0}}. \tag{4.2d}$$

The equilibrium irreversible diapycnal diffusivity (averaged over a finite-time period in the equilibrium stage) is strongly dependent upon R_ρ, which is the only non-dimensional parameter that varies significantly in oceanographic environments. In table 3 we show explicitly the equilibrium irreversible diapycnal diffusivities for heat and salt (K_Θ^{irr}, K_S^{irr}) as well as the irreversible flux ratio γ^{irr} for each of 10 different values of R_ρ. These irreversible diapycnal diffusivities are consistent with the traditionally defined diapycnal diffusivities obtained in previous three-dimensional simulations with similar resolutions (Traxler *et al.* 2011; Radko & Smith 2012). The functional dependence of K_Θ^{irr} and γ^{irr} on R_ρ can be well fit using the specific forms:

$$K_\Theta^{irr} = \frac{a}{(R_\rho - 1)^b R_\rho^c}, \quad (a = 78.09, b = 0.52, c = 0.87), \tag{4.3a}$$

$$\gamma^{irr} = aR_\rho^3 + bR_\rho^2 + cR_\rho + d, \quad (a = -0.00068, b = 0.0163, c = -0.125, d = 0.77), \tag{4.3b}$$

$$K_S^{irr} = \frac{K_\Theta^{irr}}{\gamma^{irr}} R_\rho. \tag{4.3c}$$

Both the data and our fitting results are displayed in figure 5. The expression for K_Θ^{irr} we employ is based upon the assumption that K_Θ^{irr} goes to infinity as R_ρ approaches 1 and K_Θ^{irr} goes to 0 as R_ρ goes to infinity (when salt fingers are extremely weak). We use a

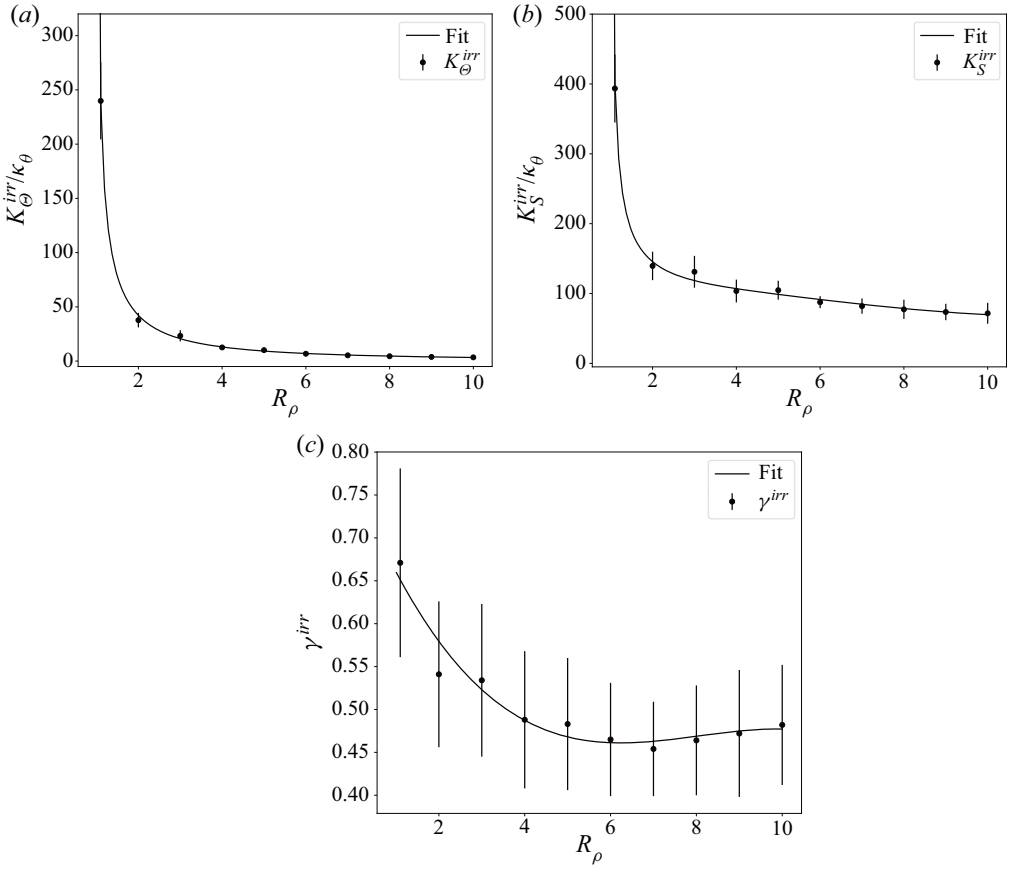

Figure 5. Averaged K_Θ^{irr} (*a*), K_S^{irr} (*b*) and γ^{irr} (*c*) over the statistical equilibrium state as a function of R_ρ from unbounded model simulations (simulation numbers 1–10). Numerical fitting of (4.3) is shown in each figure to be compared with the data.

third-order polynomial form for γ^{irr} in order to capture the transition from a decreasing γ^{irr} to increasing γ^{irr}, as shown in figure 5(*c*). It is worth noting that these expressions differ from the expressions suggested by Radko & Smith (2012), in which simulations have been performed over a much more restricted range of R_ρ ($1 < R_\rho < 3$) to which the similarity theories described in Radko (2008) could be applied.

4.2. *Direct numerical simulation results for the interface model*

4.2.1. *Time evolution of simulations for the interface model*

As in the case of the unbounded gradient model, we will begin our discussion of the interface model by first providing an overall description of the evolution of the system.

Figures 6(*a*) and 6(*b*) display the evolution of temperature induced buoyancy flux $\mathcal{H}_\Theta$ and minus salinity induced buoyancy flux $-\mathcal{H}_S$ at each depth on a logarithmic scale from our simulation with initial density ratio $R_{\rho 0} = 2$. The fluxes firstly develop around the midpoint of the interface where the background gradients are steepest and then extend to the physical boundaries of the computational domain, a process that is accompanied by the growth and expansion of the fingering-affected region as visualized in figure 6(*c*,*d*).

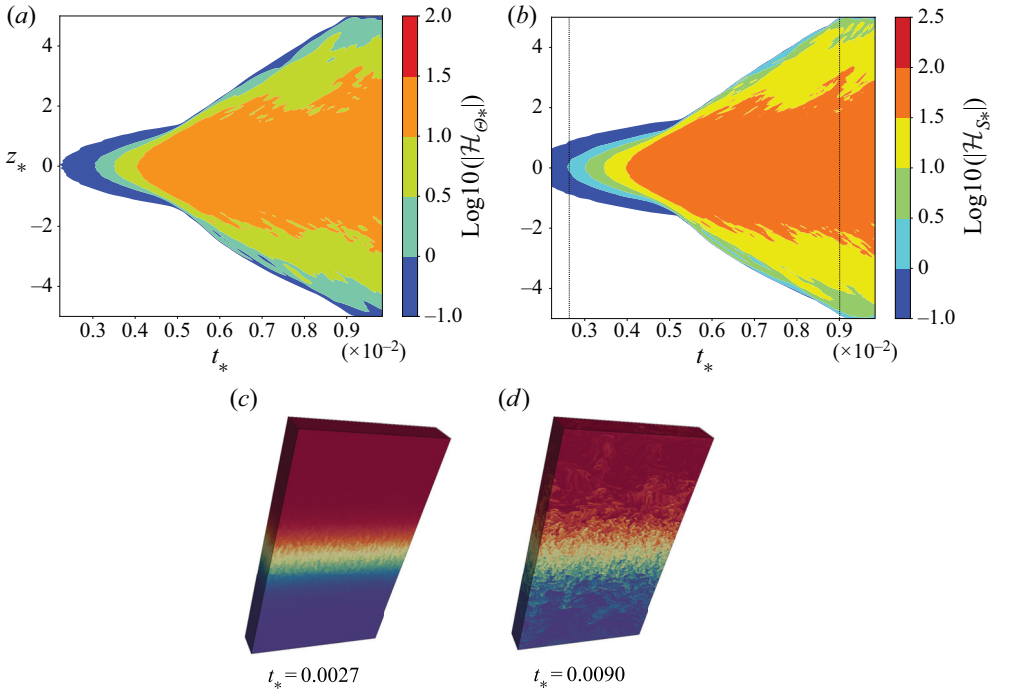

Figure 6. (*a*,*b*) Contour plot of $\mathcal{H}_\Theta$ and $\mathcal{H}_S$ in the simulation case 11. (*c*,*d*) Snapshots of salinity fields taken at two time slices of the simulation, note that the axis scales in (*c*) and (*d*) have been adjusted for better visualization purposes.

The fingers appear to be more abundant and narrower than those depicted in figure 4 due to the much larger domain in which we have elected to simulate salt-fingering turbulence in the interface model.

It is clear that at the time the simulation is arrested the fluxes are still extending vertically in space and have begun to be confined by the upper and lower boundaries of the domain. Continuing the evolution of the system beyond this time would inevitably introduce effects due to boundary reflections which would render the results unphysical. Although the system as a whole is not in statistical equilibrium at this time, a quasi-equilibrium state has already been established across the region of strong background gradients that define the interface (say the region between $-2 < z_* < 2$). In this region, salt-fingering turbulence (illustrated in figure 6*b*) will be recognized as having the same characteristics as the equilibrium fingering field in the unbounded gradient model (see figure 4*f*).

4.2.2. *Reversible and irreversible buoyancy fluxes in the interface model*

Since the interface model is describing a closed system with well-defined potential energies, we are in a position to make detailed tests of the accuracy of satisfaction of the energy budget equations discussed in § 2.2 which we proceed to perform in this section.

We first illustrate the evolution of temperature/salinity potential energies (solid lines) and temperature/salinity background potential energies (dashed lines) in figure 7(*a*,*b*). In accord with the discussion in § 2.2, PE_Θ is always larger than BPE_Θ (the minimum potential energy state for temperature), the difference between which corresponds to the available potential energy APE_Θ which is able to be released back to the kinetic energy reservoir. In figure 7(*b*) the salinity potential energies are decreasing, with

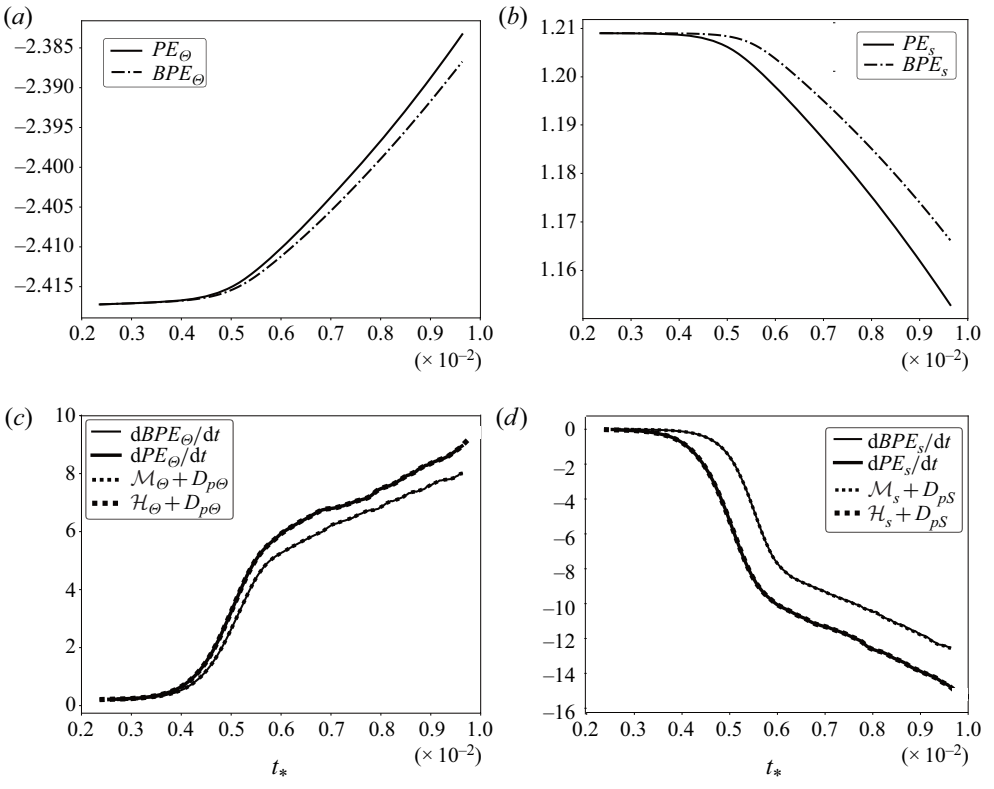

Figure 7. Time evolution of temperature potential energy (*a*) and salinity potential energy (*b*) of simulation case 11. Test of the potential energy budget equations for PE_Θ, BPE_Θ(*c*), as well as PE_S and BPE_S (*d*).

BPE_S (the maximum potential energy for salinity) being always larger than PE_S. The differences between PE_S and BPE_S correspond to the quantity of potential energy that may be 'returned' from the kinetic energy reservoir. The evolution of $PE_S(PE_\Theta)$ and $BPE_S(BPE_\Theta)$, as discussed in § 2.2, should follow (2.8) and (2.12) if the system is a closed system. This is tested in figure 7(*c*,*d*), where the time derivative of potential energies are plotted as solid lines to compare with their predicted contributions $\mathcal{H} + D_p$ and $\mathcal{M} + D_p$ calculated from their definitions in (2.9) and (2.12). Solid and dashed lines agree well which each other in figure 7(*c*,*d*), indicating that the above equations have been obeyed quite well in our numerical simulations. Such agreement also reveals that the current resolution implemented in our DNS is high enough to precisely capture the critical influence of small-scale diffusion.

Although it may seem that the irreversible fluxes are always weaker than the traditionally defined fluxes within the simulation time (shown in figure 7*c*,*d*), it is not the case if we compare the irreversible fluxes and traditional fluxes within a finite region near the centreline shown in figure 8 (we choose to focus upon the range $-2 < z_* < 2$ in this case). The evolution of fluxes in this region strongly resembles the evolution process in the unbounded gradient model: there are also evident phase delays in the irreversible fluxes (more evident phase delays in the salinity fluxes than temperature) in the early evolution of the flow, after which both definitions tend to agree with each other once the system enters a statistically steady state. This demonstrates that the system has already reached a quasi-equilibrium state across the width of the transition layer ($-2 < z_* < 2$)

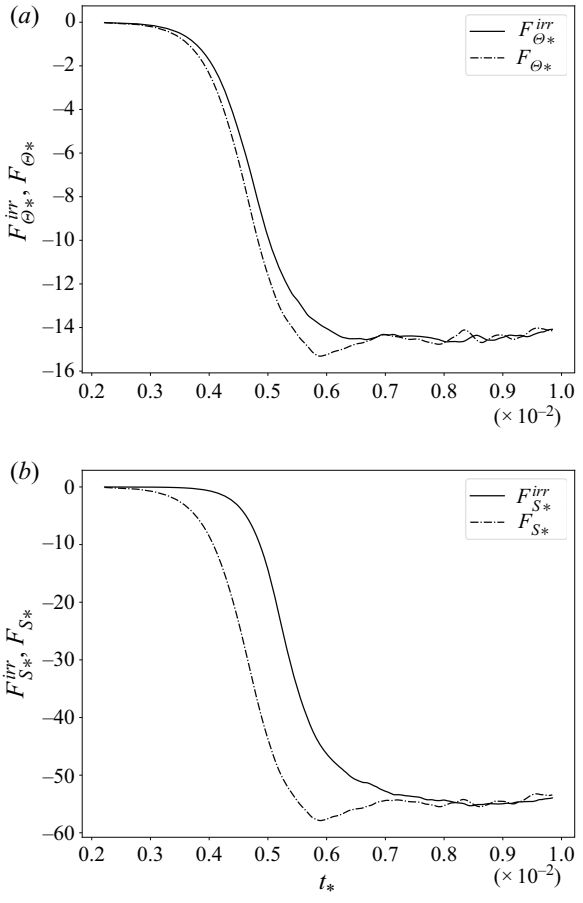

Figure 8. Comparison of the evolution of F_Θ and F^{irr}_Θ (*a*) as well as F_S and F^{irr}_S (*b*) averaged over the centreline region $-2 < z_* < 2$.

(such agreement only occurs in the statistical equilibrium state as shown in our analysis of results from the unbounded gradient model). The irreversible fluxes are generally smaller than the traditional fluxes while salt fingers continue to grow in the outer regions of our domain, averaging over the entire domain will still lead to smaller irreversible fluxes as seen in figure 7(*c*,*d*).

The above discussions rely upon an important assumption that lies at the core of the present paper, namely that the evolution of salt-fingering turbulence in a local region in the interface model can be understood on the basis of our simulations of salt-fingering turbulence in the unbounded gradient model. Different regions (with different vertical positions) may have different growth rates or different fingering widths, but, we hypothesize, they always follow the same path of turbulence evolution that we have shown to obtain in the unbounded gradient model at the same density ratio. If this hypothesis is correct it both suggests that the local irreversible fluxes will be smaller than traditional fluxes in the finger growth stage (with a phase delay), and that the local equilibrium stage can be characterized by coincidence between the reversible and irreversible fluxes. This hypothesis will be directly tested and established as correct in the

next subsection where we will apply the parameterization of diapycnal diffusivity obtained through analysis of data from the unbounded gradient model to the interface model.

4.2.3. *Effective diapycnal diffusivity for the interface model*

The manner in which we calculate this important quantity for the interface model is necessarily distinctly different than the simple method employed to compute diapycnal diffusivity for the unbounded gradient model. First, the interface model is inhomogeneous vertically and there is always stronger flux near the centre of the interface compared with boundary regions, as clearly shown in figure 6(*a*). Secondly, no equilibrium state exists in this run-down experiment, and, thus, both the fluxes and the related diapycnal diffusivity are essentially time-dependent. Previous researchers (e.g. Kimura *et al.* 2011) computed averages of the fluxes over the interface region as well as a time average over periods during which the buoyancy Reynolds number did not vary significantly to obtain a value for a flux which depends primarily on the non-dimensional parameters of the initial profiles. They further employed the functional dependence so determined to obtain a representation of diapycnal diffusivity dependent upon both R_ρ and Ri in circumstances in which the system is also influenced by shear. In the current work, however, we argue that averaging over a finite region near the centre of the interface will inevitably introduce large errors in the inference of diapycnal diffusivity by implying that there are large variances in both the local density ratios and local fluxes in the averaging region. Explicitly, the density ratio and diapycnal diffusivity as a function of depth defined by the horizontal average of the temperature and salinity fields are as follows:

$$R_\rho(z) = \frac{\alpha \bar{\Theta}_z}{\beta \bar{S}_z}, \tag{4.4a}$$

$$K_\Theta(z) = -\frac{F_\Theta(z)}{\bar{\Theta}_z}, \tag{4.4b}$$

$$K_S(z) = -\frac{F_S(z)}{\bar{S}_z}. \tag{4.4c}$$

It will be observed that the above formulae are based on the traditionally defined diapycnal diffusivity. As discussed in § 4.2.2, the irreversible fluxes equilibrate to the same value as the traditionally defined fluxes in the statistical equilibrium state. Since our focus will be on the equilibrium properties in this subsection, such distinctions will be irrelevant in the following discussion. In figure 9(*a*) we show the vertical variations of $R_\rho(z)$ at the centreline region for our simulation number 11. Although $R_\rho(z)$ is initialized to be $R_{\rho 0} = 2$ for all depths, the system evolves into a state in which R_ρ is depth dependent. The difference between local $R_\rho(z)$ and the initially specified global value is especially significant near the centre of the interface model, with $R_\rho(z_* = 0)$ being much larger than 2 and $R_\rho(z_* = -2), R_\rho(z_* = 2)$ much smaller than 2. This pattern does not rely on the time chosen as demonstrated in figure 9(*b*) in which we have plotted the evolution of $R_\rho(z)$ at each of these three positions as a function of time. As the system approaches the statistical equilibrium state appropriate to a specific depth, the $R_\rho(z)$ also attains a quasi-equilibrium value. In figure 9(*b*) the equilibrium value of R_ρ is shown to be larger than $R_{\rho 0}$ near the centre of the interface model but smaller than $R_{\rho 0}$ at $z_* = 2, -2$ whose heights are displaced from the centreline. This pattern arises as the first-order response to the spatial distribution of fluxes shown in figure 6. As strong heat and salt fluxes in the central region of the interface support a strong flux of both heat and salt downwards across the

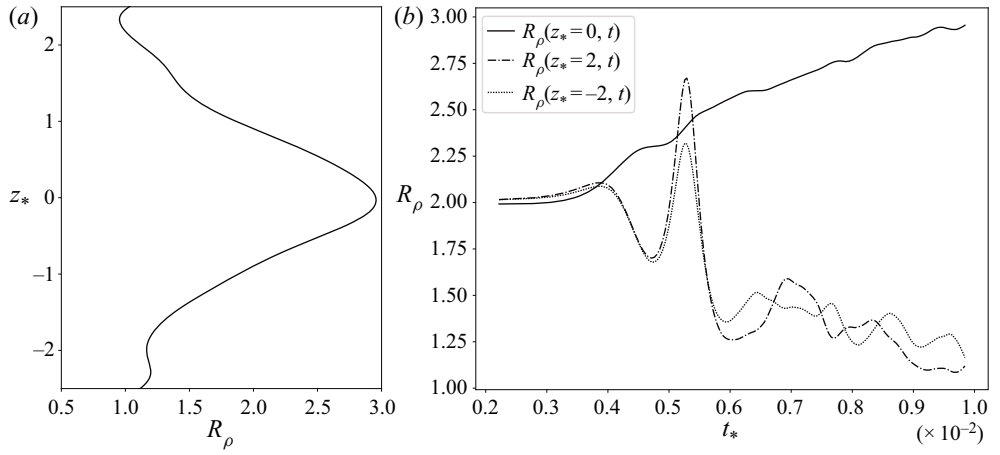

Figure 9. (*a*) Local R_ρ near the centreline region at $t_* = 0.098$ for simulation number 11. (*b*) The time-dependence of local R_ρ at $z_* = 2$, $z_* = 0$ and $z_* = -2$.

centreline, both temperature gradient Θ_z and salinity gradient S_z decrease in the vicinity of $z_* = 0$. Since this effect is stronger for salinity than for temperature (salt fluxes are stronger in a salt-fingering process), $R_\rho = \alpha\bar{\Theta}_z/\beta\bar{S}_z$ at the centreline will increase because of the more prominent decrease in the denominator than the numerator. For the $z_* = 2$ region (the same argument applies for $z_* = -2$), however, these regions will experience an increase in both S_z and Θ_z, as both salinity and temperature below $z_* = 2$ are delivered downwards across the centreline, while salinity and temperature above $z_* = 2$ remain relatively unchanged (fluxes are much smaller away from the centreline). This effect is also stronger in the salinity field than in the temperature field, leading to a decrease in R_ρ at $z_* = 2$ (the denominator is increasing more strongly). The same mechanism leads to a density inversion zone (with $R_\rho < 1$) in regions further removed from the centre of the transition region (not shown). Such regions have been previously reported and discussed in the two-dimensional numerical simulations of Shen (1989), Shen & Veronis (1997) and Singh & Srinivasan (2014), but further discussion of these regions is beyond the scope of the present paper.

These large variations with R_ρ as a function of depth indicate that, instead of averaging over a particular depth range (as in Kimura *et al.* (2011)) in which R_ρ varies so intensely (the diapycnal diffusivities and flux ratio evaluated using this method are discussed in appendix B), it would appear to be a better strategy to treat each depth separately, especially insofar as diapycnal diffusivity is concerned. These diapycnal diffusivities do vary significantly as a function of depth, as shown by the solid lines in figure 10. Specifically, we plot in figure 10(*a–c*) the evolution of K_θ,K_s (both non-dimensionalized by dividing by the molecular diffusivity κ_θ) and the flux ratio γ at several different depths. It is apparent that the diffusivities at different local depths tend to fluctuate about different values. It is then a well-motivated assumption to make that the diapycnal diffusivities at depth z are controlled by the local density ratio $R_\rho(z)$. To test this hypothesis, we apply the parametrization schemes developed on the basis of results from the unbounded gradient model (4.3) to the $R_\rho(t)$ data at different depths and also plot these data on figure 10(*a–c*) separately as the dashed curves. These dashed curves should be understood as representing the equilibrium diapycnal diffusivities of the turbulence at a particular value of R_ρ at the corresponding time. It will be observed that there is a generally good match between the dashed curve and the solid curve. Specifically, the dashed curve gives a

more accurate prediction at $z_* = 0$, where R_ρ is in a relatively stationary environment which better resembles the settings of the unbounded gradient model. At $z_* = 2$ and $z_* = -2$, both the solid and dashed curves have large variations due to strong local flux fluctuations, however, the two curves are varying around similar equilibrium levels, which reveals their connections. These results supports the validity of our hypothesis that we can accurately treat the local (depth dependent) environment of the interface model as a particular realization of the unbounded gradient model from which local fluxes for the interface model can be determined from the local value of R_ρ.

5. Salt-fingering parametrization schemes for application in the ocean component of global climate models

In the previous sections of this paper we have described the results obtained on the basis of direct numerical simulations of a salt-fingering system in the unbounded gradient model at $\tau = 0.01$ and $Pr = 7$. On the basis of these results we have been able to determine the diapycnal diffusivities for temperature and salt as a function of R_ρ. We have furthermore shown that in a statistical equilibrium state of the salt-fingering system with inhomogeneous temperature and salinity gradients as a function of depth, the local fluxes (either irreversible flux or the more commonly defined flux) can be very closely predicted by applying this functional relationship based upon the local density ratio R_ρ. It is then a natural question as to how such a DNS-based flux law would behave if it is employed to parameterize the influence of salt-fingering turbulence in a global ocean model to represent the diapycnal diffusivities for heat and salt in terms of the large-scale fields defined on the low-resolution model grid. We address this question in what follows.

There have been different proposals previously suggested as to how the influence of salt-fingering turbulence should be represented in large-scale models of the general circulation of the oceans.

One of the first of these was a component of the Kappa profile parameterization of Large, McWilliams & Doney (1994). Specifically, the diffusivities for heat and salt in this parameterization were based on applying the laboratory 4/3 power law (e.g. Turner 1967; Schmitt 1979; McDougall & Taylor 1984) to C-SALT observations of Schmitt (1988), based upon the mathematical representations:

$$K_S(R_\rho) = \left[1 - \left(\frac{R_\rho - 1}{0.9}\right)^2\right]^3 \times 10^{-3}\ \mathrm{m^2\ s^{-1}} \quad (1 < R_\rho < 1.9), \tag{5.1a}$$

$$K_\Theta(R_\rho) = \frac{0.7}{R_\rho} K_S \quad (1 < R_\rho < 1.9). \tag{5.1b}$$

Zhang, Schmitt & Huang (1998) later applied a somewhat modified mathematical representation of the R_ρ dependence of the fluxes in the salt-fingering system in sensitivity tests of the form previously suggested by Schmitt (1981) as

$$K_S(R_\rho) = \frac{1}{1 + \left(\dfrac{R_\rho}{1.6}\right)^6} \times 10^{-4}\ \mathrm{m^2\ s^{-1}} + K_b, \tag{5.2a}$$

$$K_\Theta(R_\rho) = \frac{0.7}{R_\rho}(K_S - K_b) + K_b, \tag{5.2b}$$

in which $K_b = 3 \times 10^{-5}\ \mathrm{m^2\ s^{-1}}$.

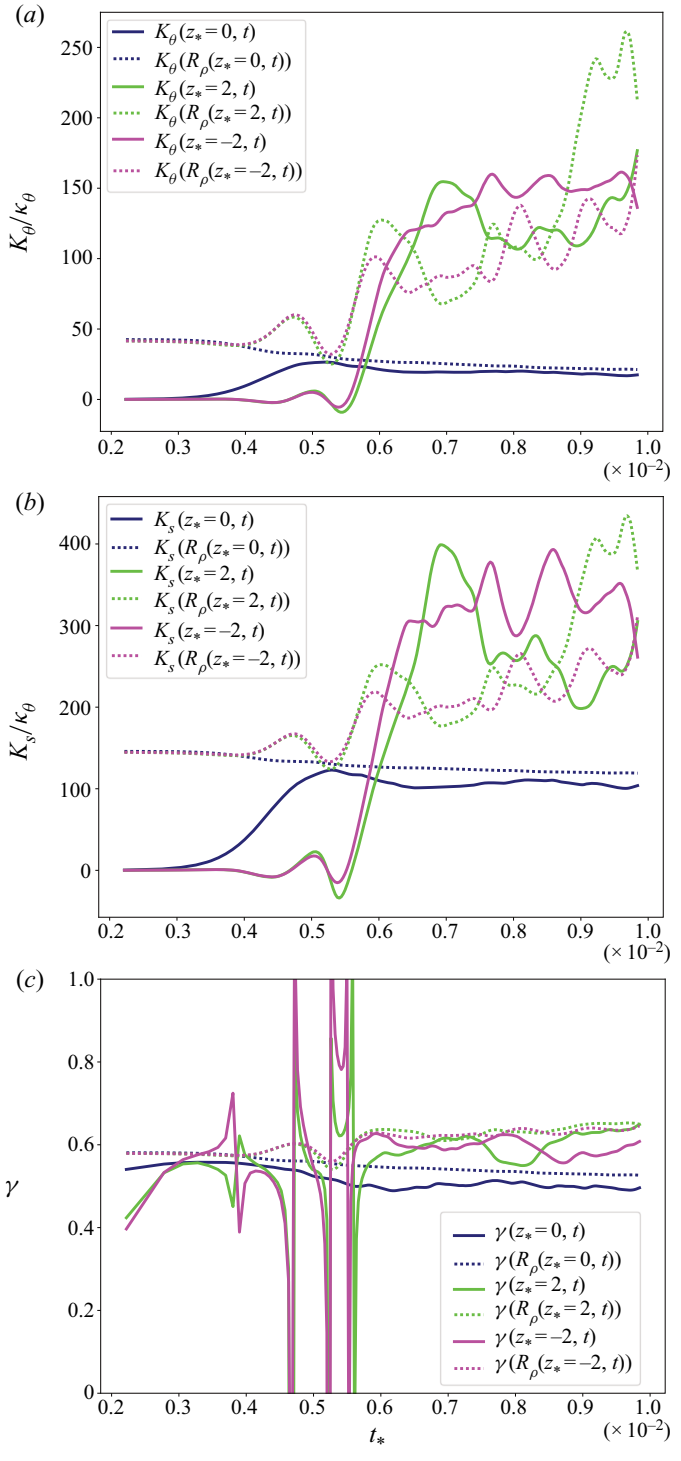

Figure 10. Time evolution of diapycnal diffusivities for temperature K_θ (a) and salinity K_S (b), as well as flux ratio $\gamma(c)$ at $z_* = 2$, $z_* = 0$ and $z_* = -2$. In each figure, the solid line represents data from the interface model and the dashed line represents the prediction of K_θ, K_s, as well as γ calculated by applying our new parametrization method to the time evolution of local R_ρ shown in figure 9(b).

The more widely used parametrization at present is based upon empirical fits of the mathematical form (5.1*a*) to the most recent ocean observations from the NATRE experiment described in St. Laurent & Schmitt (1999), which has delivered the explicit forms:

$$K_S(R_\rho) = \left[1 - \frac{R_\rho - 1}{1.55}\right]^3 \times 10^{-4}\ \mathrm{m^2\ s^{-1}} \quad (1 < R_\rho < 2.25), \tag{5.3a}$$

$$K_\Theta(R_\rho) = 0.7\left[1 - \frac{R_\rho - 1}{1.55}\right]^3 \times 10^{-4}\ \mathrm{m^2\ s^{-1}} \quad (1 < R_\rho < 2.25). \tag{5.3b}$$

Such parameterizations have since been routinely applied in the parallel ocean program (POP) and parallel ocean program 2 (POP2) of Smith *et al.* (2010) as the salt-fingering parametrization. The more recent community ocean vertical mixing project (CVMix project Griffies *et al.* (2015)), which has been designed to be implemented in a variety of ocean models such as the model for prediction across scales-ocean (MPAS-ocean) and the modular ocean model (MOM), also represents vertical mixing associated with the salt-fingering turbulence process using the same mathematical representations. It is clearly of interest to compare the parameterization scheme we have developed based upon DNS-based simulations of salt-fingering turbulence to these empirically based representations. To this end, comparisons are presented in figure 11 of these empirically derived parameterizations with our DNS results. In figure 11(*a*) the DNS-based parametrization scheme is represented by the dash–dotted line and the NATRE data-based parametrization scheme by the solid line. Figure 11(*b*) further displays the original NATRE data (for which R_ρ is restricted to the range 1.3 to 1.8) which is used to obtain (5.3*a*). These two parametrization schemes do not deviate significantly within the range of 1.3 to 1.8, but do differ significantly for both small R_ρ and large R_ρ. The fact that the DNS-derived data are close to the experimental data within the range 1.3 to 1.8 means that the discrepancies between the two parametrization schemes may be largely due to the specific mathematical forms to which the experimental observations are fit, a procedure that is liable to lead to large errors in regions of parameter space not actually sampled by the observations. One strength of the data-based parametrization derived from direct numerical simulations of salt-fingering turbulence is that the parameterization is subject only to error based upon the adequacy of the resolution of the turbulence.

It is informative for the purpose of further comparing the data-based parameterization scheme with the empirical scheme to consider the interface model to represent the depth-dependent oceanographic conditions to be parameterized.in terms of the diapycnal diffusivities to be inferred. For this purpose, we will focus upon the interface region itself in which statistical equilibrium conditions have been obtained in our simulations. In non-dimensional vertical coordinate terms this is the region $-2.5 < z_* < 2.5$ (see figure 6). Such comparisons made for simulation number 11 at $t_* = 0.098$ are shown in figure 12. It can be seen from this figure that the DNS-based parametrization scheme is characterized by an improved fit to the true diapycnal diffusivities calculated from the simulation data within the region $-2 < z_* < 2$. The mismatch of both parametrization schemes beyond this region is possibly a consequence of the fact that the system had yet to reach a quasi-equilibrium state there (see our discussions in § 4.2.2). The most inaccurate region of the NATRE-based parametrization scheme is the prediction of diapycnal diffusivities near the centre of the transition layer: both K_Θ and K_S are set to 0 in this region based on (5.3*a*) since the local R_ρ is above 2.55, while the actual diapycnal diffusivities are 0.03 $\mathrm{cm^2\ s^{-1}}$ for temperature and 0.1 $\mathrm{cm^2\ s^{-1}}$ for salinity.

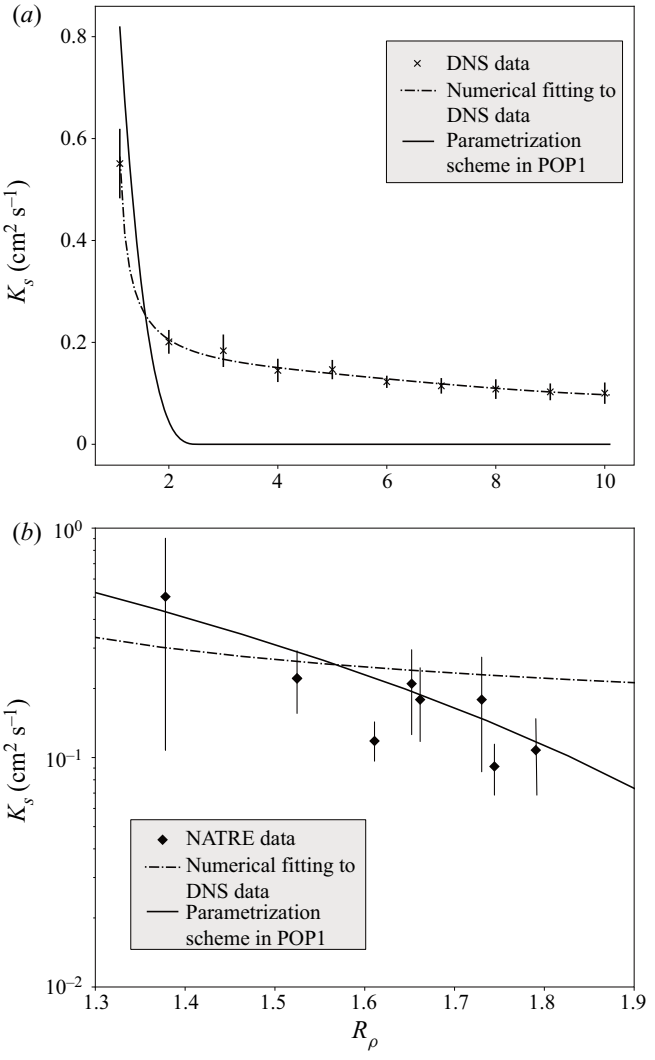

Figure 11. Comparison of parametrization of diapycnal diffusivity for salt K_s implemented in POP1 ocean model based on the NATRE experiment (St. Laurent & Schmitt 1999) and DNS-based turbulent flux laws obtained from our DNS. Note that (*b*) is the zoom in of (*a*) with logarithm scale on diffusivities in order to show explicitly the original data from the NATRE experiment.

Although the above analysis demonstrates significant advantages of the DNS-based parametrization scheme over the NATRE-based parametrization scheme, caution is necessary when applying this parametrization scheme in a climate model. First it must be recognized that this scheme is intended only to represent the diapycnal mixing caused by homogeneous salt-fingering turbulence unaffected by the action of secondary instability processes. One of the best known of such secondary effects involves the formation of thermohaline staircases (possibly developed through the secondary γ-instability of Radko (2003); Stellmach *et al.* (2011)). When such staircases form, the result may be a significant increase of the local fluxes of heat and salt through the formation of high-gradient interfaces. Such structures always form when the local density ratio R_ρ is small, but their formation does not depend solely upon the single parameter R_ρ: rather

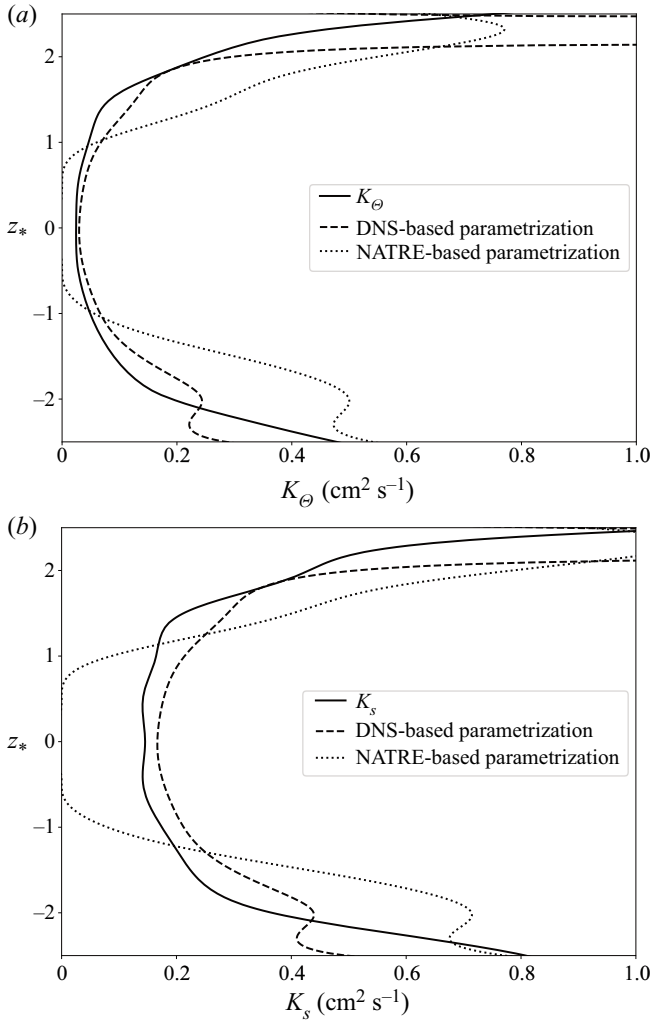

Figure 12. A comparison of the performance of DNS-based parametrization scheme (dashed curve) and the NATRE-based parametrization scheme (dotted curve) for both heat diapycnal diffusivities (*a*) and salt diapycnal diffusivites (*b*).

there is observational evidence of both staircases (Schmitt *et al.* 2005) and staircase-free salt-fingering fields (St. Laurent & Schmitt 1999) in which the density ratio R_ρ is in the same range. Our DNS-based parametrization scheme is applicable in the latter case since no secondary structures have formed in the simulations we have described.

Secondly, we have not included the interaction between the salt-fingering fields with any background internal wave strain that might be expected to exist ubiquitously in the natural marine environment. Early work of Schmitt & Evans (1978) suggested that salt-fingering field turbulence would not have time to establish if the system is intermittently perturbed by internal wave strain whose frequency is significantly higher than the salt-fingering growth rate. Their calculation suggested that in order for the salt-fingering growth rate to exceed the local buoyancy frequency N, the density ratio R_ρ would have to be smaller than 2. This idea has been supported by the water-tank experiments of Wells & Griffiths (2003) which suggest that the effective vertical diffusivities of heat and salt would be

strongly suppressed by the intermittency of the turbulence involved. It is for this reason that the NATRE empirically based salt-fingering parametrization scheme abruptly sets diapycnal diffusivities to 0 when R_ρ is larger than the critical value $R_\rho^0 = 2.55$. However, the direct numerical simulations of Kimura *et al.* (2011) reveal a different aspect of the interaction between salt fingerings and internal wave strain. For a system that is susceptible to both Kelvin–Helmholtz instability (that is induced by internal wave shear) and salt fingering simultaneously, it is suggested that the diapycnal diffusivities and flux ratios are more strongly influenced by salt-fingering instabilities in the mixed system. This suggests that salt fingering engendered turbulence may be more robust to disruption by internal wave strain than it has been observed to be in laboratory experiments. We expect that such subtleties will be resolvable in future direct numerical simulations in a much larger domain which captures the complete life cycle of internal wave strains in a salt-fingering-favourable environment. These might be expected to add dependence upon an additional non-dimensional parameter to the parameterization, namely the buoyancy Reynolds number Re_b.

6. Summary and conclusions

In the oceanographic double-diffusion system where density is simultaneously influenced by both temperature and salinity, understanding the behaviour of turbulent fluxes has always constituted the core of studies of such processes, whether these involve the salt-fingering process or the diffusive convection counterpart in which cold fresh water lies above warm salty water. However, the previously employed definition of heat flux and salt flux is one that has included the influence of both reversible 'stirring' and irreversible mixing, while only an irreversible process may contribute to the turbulent diapycnal diffusivities which are employed to represent the impact of such small-scale turbulence in large-scale models. In this paper we have developed a theoretical framework which enables us to separate the background potential energy into two different reservoirs, namely a temperature related potential energy reservoir and a salinity related potential energy reservoir. In each of these two reservoirs, we further separate the energies into background potential energy and available potential energy in the same way as in Caulfield & Peltier (2000) and Peltier & Caulfield (2003): background potential energies are defined as the minimum (maximum) potential energies for all possible configurations of the temperature (salinity) field that can only increase (decrease) due to irreversible mixing in these fields. The irreversible temperature (salinity) fluxes are therefore defined as the rates of change of the temperature (salinity) related background potential energies, whose values must be calculated by sorting the temperature (salinity) fields adiabatically into the minimum (maximum) potential energy states. We have also proposed algorithms that have enabled us to properly calculate such irreversible fluxes in the unbounded gradient system with its periodic boundary conditions in the vertical direction.

Inspection of these newly defined irreversible fluxes in our direct numerical simulations have enabled us to more clearly display the nature of the irreversible fluxes in the salt-fingering fields. There is little irreversible salt flux when the salt fingers are exponentially growing in height, instead, irreversible salt flux rapidly rises when salt fingers are 'broken' by the secondary zig-zag instability. This is a completely different signature compared with the traditionally defined fluxes which grow when fingers grow and decay when fingers are broken. In fact, the formation of salt fingers is for the most part an intrinsically reversible process in salt-fingering fields since there can exist an ideal adiabatic process which returns fluid parcels at the fingertips back to their original

positions so as to almost reset the salt field to its original state (although this will not happen in a natural salt-fingering system), but no adiabatic process can return the salt field to its initial state when the high-salinity fluid in the fingers exchanges salt with its much fresher neighbours at the time when fingers are twisted and broken by the zig-zag instability. In the equilibrium state where the salt-fingering growth process is balanced by the salt-fingering disruption process (see Radko & Smith 2012), the irreversible fluxes will equilibrate to the same value as the equilibrium value for the traditionally defined fluxes, except that there is an apparent time delay in the fluctuations of the irreversible fluxes compared with the traditionally defined fluxes. It is for this reason that the distinction between the irreversible fluxes and reversible fluxes are not vital in our discussions regarding statistical equilibrium values of the fluxes. However, we expect that the necessity of the distinction between reversible and irreversible mixing will be of profound importance to a detailed understanding of salt-fingering instability in the presence of background shear, a problem to which we will turn our attention in future work.

Our direct numerical simulations have also enabled very important insights into the physical processes involved in the evolution of salt-fingering turbulence in an inhomogeneous system. In our simulations of salt-fingering turbulence in the interface model initiated with hyperbolic-tangent profiles, we have shown that fluxes (either traditionally defined fluxes or irreversible fluxes) at different depths in the transition region follow the evolutionary trajectory as do fluxes in the homogeneous system. Such a path has been shown to consist of three stages based upon our simulations in the unbounded gradient model (as previously discussed in Shen (1995) and Traxler *et al.* (2011) for example), namely the stage of finger growth, the stage of finger disruption by the zig-zag instability and the equilibrium stage. Regions near the centre of the interface layer experience faster fingering growth and reach equilibrium much earlier than the regions closer to the boundaries of the interface layer since temperature and salinity gradients are much sharper near the layer centre. These fluxes will in turn modify the local temperature and salinity gradients, leading to the establishment of different equilibrium density ratios R_ρ at different depths (larger than $R_{\rho 0}$ at the centre and smaller than $R_{\rho 0}$ away from the centre). The equilibrium fluxes at these different depths were further shown to be well predicted by the flux laws acquired from the unbounded gradient model which are solely dependent on local density ratio R_ρ. In this way, these distinctly different models that have been used to represent salt-fingering turbulence in different physical situations (see Radko 2013) are shown to be intimately connected.

An important application of the analyses we have performed is that the results have enabled us to develop an original data-based parameterization of salt-fingering turbulence for use in the ocean component of large-scale climate models. A recent paper in the physical oceanography and climate literature in which the influence of the parameterization of doubly diffusive turbulence on the large-scale oceanographic circulation is that of Peltier, Ma & Chandan (2020). Compared with existing parametrization schemes based on empirical fits to data derived from ocean observations, the DNS-based parametrization is based upon a much clearer physical understanding and is characterized by much smaller error bars on the fluxes being parameterized. This is simply a consequence of the fact that the diapycnal diffusivities associated with homogeneous salt-fingering turbulence can be thoroughly understood, precisely calibrated and well tested. The additional steps that will lead to further improvements to the parametrization scheme will require identification and quantitative characterization of the influence of different secondary instabilities. We expect that DNS will continue to provide

an invaluable tool for the development of the needed parameterization schemes for use in lower resolution models.

Acknowledgements. The computations on which this paper is based were performed on the Niagara cluster at the SciNet High Performance Computing facility at the University of Toronto funded by the Canadian Foundation for Innovation, the Province of Ontario and the University of Toronto. SciNet is a component of the Compute Canada HPC platform. The research of W.R.P at University of Toronto is supported by NSERC Discovery grant A9627. We are grateful to Hesam Salehipour for helpful discussions when the work described in this paper was in the initial planning stage.

Declaration of interest. The authors report no conflict of interest.

Author ORCIDs.
Yuchen Ma https://orcid.org/0000-0002-5829-6196.

Appendix A. Numerical resolution requirements for the direct numerical simulations

The smallest scale that could require resolution for the salt-fingering system is the Batchelor scale (Batchelor 1959) for salinity dissipation which is defined as

$$B_s = (\nu\kappa_s^2/\epsilon)^{1/4}, \tag{A1}$$

in which ν is kinematic viscosity, κ_s is the molecular diffusivity for salinity and $\epsilon = 2\nu\langle e_{ij}e_{ij}\rangle$ is the average rate of kinetic energy dissipation per unit mass of fluid. As this scale is extremely small under oceanographic conditions ($Pr = 7$, $\tau = 0.01$) and is barely accessible in DNS, simulations in this paper have employed a resolution which is slightly coarser but of the same order as the Batchelor scale for both the unbounded gradient model and the interface model.

For simulations using the unbounded gradient model, we have employed the resolution of $385 \times 385 \times 770$ grid points for simulation numbers 1–7 and a slightly lower resolution of $266 \times 266 \times 532$ grid points for simulation numbers 8–10. The corresponding grid intervals (equal for all three coordinate directions) are displayed by circled points in figure 13 to be compared with the Batchelor scale B_s calculated at each value of R_ρ. Although B_s for the equilibrium salt-fingering field is only 2 to 5 times smaller than the grid interval currently employed, an order of magnitude more grid points would be required in order to fully resolve B_s in each of three spatial dimensions, which is not possible due to our limited numerical capability. Fortunately, both the irreversible and the traditionally defined fluxes are not sensitive to resolution at this level, which is illustrated in figure 14. In the figure we compared the flux evolution trajectory from our simulation number 2 ($385 \times 385 \times 770$ grid points) with a test simulation with the same conditions except for a much lower resolution ($175 \times 175 \times 350$ grid points with grid interval as 0.00286). Figure 14 shows that the flux trajectory is still following almost the same trajectory with the simulation discussed in the main text even at such a low resolution, demonstrating that the flux trajectory discussed in the main text is robust. Therefore, the resolution employed for the unbounded gradient model simulations is already sufficiently high within the scope of our discussions in the current paper.

For simulations using the interface model, the large simulation domain ($30\ FGW \times 5\ FGW \times 100\ FGW$) requires a large number of grid points to be employed. In order to improve the accuracy of these demanding simulations, we have performed three test runs for each simulation number 11, 12 and 13 at a coarse resolution of $420 \times 35 \times 1400$ grid points (other settings are kept the same) to decide the most suitable design for the simulation grids. In these test runs the horizontally averaged kinetic energy dissipation

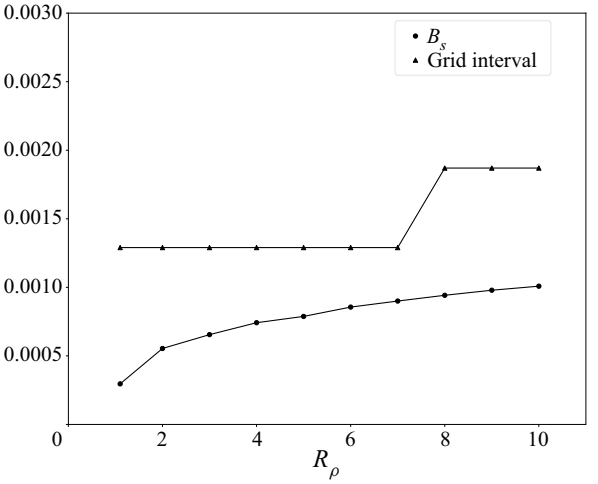

Figure 13. A comparison of B_s at the equilibrium stage and the resolution that is actually employed in simulation numbers 1–10 under the unbounded gradient model.

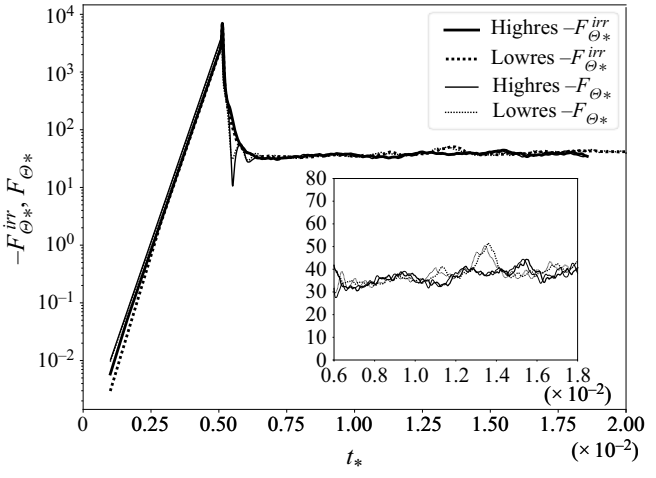

Figure 14. Evolution of F_Θ as well as F^{irr}_Θ under the unbounded gradient model for $R_\rho = 2$ at two different resolutions: $385 \times 385 \times 770$ (solid curve) and $175 \times 175 \times 350$ (dashed curve). Simulations under these two resolutions display a similar evolution trajectory and equilibrium value for both F_Θ and F^{irr}_Θ.

rate $\bar{\epsilon}$ at different depths has been calculated for the entire life cycle to determine the largest $\bar{\epsilon}$ of the life cycle as a function of depth. The Batchelor scale needed at each depth can then be calculated from (A1), as shown in the dotted curve in figure 15 (where the example is given only for simulation number 11, the procedure discussed hereafter has also been applied for simulation numbers 12 and 13). Based on this, an ideal grid (the dot–dashed curve) was first designed to fully resolve the Batchelor scale at the relatively small cost of grid points being employed. Then we coarsen this resolution by a factor of 3.3 to reach a more realistic set of grids that can be computed within a reasonable amount of time with our current computational resources. Explicitly, while the grids are uniformly spaced in the x and y directions to 1582 and 266 intervals, the region within the height range $-1.5 < z_* < 1.5$ are taken to be more finely resolved by 1568 grid points in the

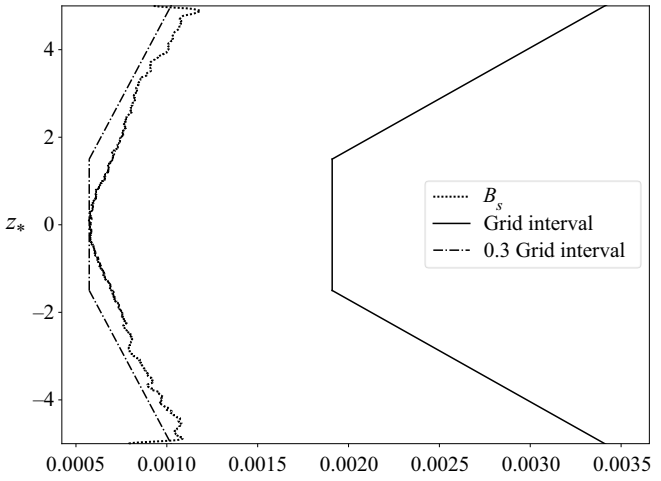

Figure 15. A comparison of the depth-dependent B_s obtained from the test simulation and the actual grid interval employed in simulation number 11. The grid intervals in simulation number 11 are designed in such a way that a 0.3 grid interval would just be sufficiently smaller than the Batchelor scale at each vertical depth.

vertical direction. In the region above and below this innermost region the vertical spacing between adjacent elements has been gradually stretched between successive levels, leading to a total number of 1428 grid points in a vertical direction for both the upper and lower region of the domain. The effectiveness of the above resolution has been discussed in the main text: the fact that the energy budget for the salinity associated potential energy can be precisely calibrated in the numerical simulations under the interface model is suggesting that the salinity dissipation has already been accurately captured in the simulation.

Appendix B. Bulk-averaged effective diapycnal diffusivities for the interface model

As we have discussed in the main text, the depth variations of R_ρ in the interface model are so significant that we chose to treat each depth separately in the analysis of diapycnal diffusivity. In this appendix we will briefly discuss the evolution of diapycnal diffusivities calculated by taking the bulk average of the turbulence. Specifically, the bulk-averaged diapycnal diffusivities and the bulk-averaged flux ratio are defined by

$$K_\Theta^{bulk} = -\frac{\langle w'\Theta'\rangle_D}{\langle \Theta_z\rangle_D}, \tag{B1a}$$

$$K_S^{bulk} = -\frac{\langle w'S'\rangle_D}{\langle S_z\rangle_D}, \tag{B1b}$$

$$\gamma^{bulk} = \frac{\alpha\langle w'\Theta'\rangle_D}{\beta\langle w'S'\rangle_D}, \tag{B1c}$$

in which $\langle\cdot\rangle_D$ represents the volume average over a specific domain D in which the turbulence is primarily active. We choose D to be $(-2 < z_* < 2)$ based upon the flux distribution shown in figure 6 (the same D has been chosen by Kimura *et al.* (2011)).

The evolution of K_Θ^{bulk}, K_S^{bulk}, as well as γ^{bulk} for simulation number 11 (initiated with $R_{\rho 0} = 2$) are plotted in figure 16. All of these trajectories are evolving into a statistically

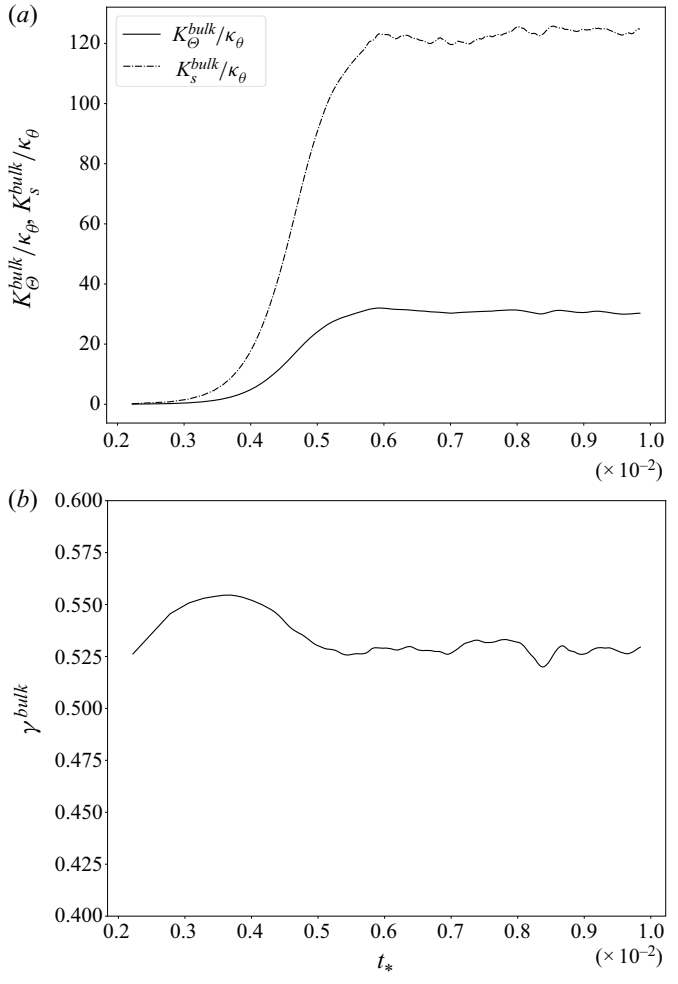

Figure 16. Evolution of (*a*) bulk-averaged effective diapycnal diffusivities for heat and salt as well as (*b*) bulk-averaged flux ratio in simulation number 11.

equilibrated state, allowing us to calculate the equilibrium values of K_Θ^{bulk}, K_S^{bulk} and γ^{bulk} by taking a time average in the equilibrated state. In the specific case of simulation number 11, the average values for (K_Θ^{bulk}, K_S^{bulk}, γ^{bulk}) over the t_* interval 0.80–0.98 is computed to be (30.5,124.3,0.528). These values are all evidently smaller than the values evaluated in the homogeneous salt-fingering turbulence (for the case of $R_{\rho 0} = 2$) listed in table 3. This comparison further strengthens our discussions in the main text: these bulk-averaged diapycnal diffusivities have systematic errors caused by the depth variations of local R_ρ and, thus, should not be used to calibrate a parametrization scheme.

References

BAINES, P.G. & GILL, A.E. 1969 On thermohaline convection with linear gradients. *J. Fluid Mech.* **37** (2), 289–306.

BATCHELOR, G.K. 1959 Small-scale variation of convected quantities like temperature in turbulent fluid part 1. General discussion and the case of small conductivity. *J. Fluid Mech.* **5** (1), 113–133.

CAULFIELD, C.P. & PELTIER, W.R. 2000 The anatomy of the mixing transition in homogeneous and stratified free shear layers. *J. Fluid Mech.* **413**, 1–47.
FISCHER, P.F., KRUSE, G.W. & LOTH, F. 2002 Spectral element methods for transitional flows in complex geometries. *J. Sci. Comput.* **17** (1–4), 81–98.
FISCHER, P.F., KRUSE, G.W., LOTTES, J.W. & KERKEMEIER, S.G. 2008 Nek5000 Web Page. Available at: http://nek5000.mcs.anl.gov.
GRIFFIES, S.M., LEVY, M., ADCROFT, A.J., DANABASOGLU, G., HALLBERG, R.W., JACOBSEN, D., LARGE, W.G. & RINGLER, T. 2015 Theory and numerics of the community ocean vertical mixing (CVMix) project. *Tech Rep*.
HOLYER, J.Y. 1984 The stability of long, steady, two-dimensional salt fingers. *J. Fluid Mech.* **147**, 169–185.
INOUE, R., YAMAZAKI, H., WOLK, F., KONO, T. & YOSHIDA, J. 2007 An estimation of buoyancy flux for a mixture of turbulence and double diffusion. *J. Phys. Oceanogr.* **37** (3), 611–624.
KIMURA, S., SMYTH, W. & KUNZE, E. 2011 Turbulence in a sheared, salt-fingering-favorable environment: anisotropy and effective diffusivities. *J. Phys. Oceanogr.* **41** (6), 1144–1159.
LARGE, W.G., MCWILLIAMS, J.C. & DONEY, S.C. 1994 Oceanic vertical mixing: a review and a model with a nonlocal boundary layer parameterization. *Rev. Geophys.* **32** (4), 363–403.
MADAY, Y., PATERA, A.T. & RØNQUIST, E.M. 1990 An operator-integration-factor splitting method for time-dependent problems: application to incompressible fluid flow. *J. Sci. Comput.* **5** (4), 263–292.
MASHAYEK, A., CAULFIELD, C.P. & PELTIER, W.R. 2017 Role of overturns in optimal mixing in stratified mixing layers. *J. Fluid Mech.* **826**, 522–552.
MASHAYEK, A. & PELTIER, W.R. 2013 Shear-induced mixing in geophysical flows: does the route to turbulence matter to its efficiency? *J. Fluid Mech.* **725**, 216–261.
MCDOUGALL, T.J. & TAYLOR, J.R. 1984 Flux measurements across a finger interface at low values of the stability ratio. *J. Mar. Res.* **42** (1), 1–14.
MIDDLETON, L. & TAYLOR, J.R. 2020 A general criterion for the release of background potential energy through double diffusion. *J. Fluid Mech.* **893**, R3.
NAKANO, H. & YOSHIDA, J. 2019 A note on estimating Eddy diffusivity for oceanic double-diffusive convection. *J. Oceanogr.* **75**, 375–393.
OSBORN, T.R. 1980 Estimates of the local rate of vertical diffusion from dissipation measurements. *J. Phys. Oceanogr.* **10** (1), 83–89.
PELTIER, W.R. & CAULFIELD, C.P. 2003 Mixing efficiency in stratified shear flows. *Annu. Rev. Fluid Mech.* **35** (1), 135–167.
PELTIER, W.R., MA, Y. & CHANDAN, D. 2020 The KPP trigger of rapid AMOC intensification in the nonlinear Dansgaard-Oeschger relaxation oscillation. *J. Geophys. Res.-Oceans*. **125**, e2019JC015557.
RADKO, T. 2003 A mechanism for layer formation in a double-diffusive fluid. *J. Fluid Mech.* **497**, 365–380.
RADKO, T. 2008 The double-diffusive modon. *J. Fluid Mech.* **609**, 59–85.
RADKO, T. 2013 *Double-Diffusive Convection*. Cambridge University Press.
RADKO, T. & SMITH, D.P. 2012 Equilibrium transport in double-diffusive convection. *J. Fluid Mech.* **692**, 5–27.
SALEHIPOUR, H., CAULFIELD, C.-P. & PELTIER, W.R. 2016 Turbulent mixing due to the Holmboe wave instability at high Reynolds number. *J. Fluid Mech.* **803**, 591–621.
SALEHIPOUR, H. & PELTIER, W.R. 2015 Diapycnal diffusivity, turbulent Prandtl number and mixing efficiency in Boussinesq stratified turbulence. *J. Fluid Mech.* **775**, 464–500.
SCHMITT, R.W. 1979 Flux measurements on salt fingers at an interface. *J. Mar. Res.* **37**, 419–436.
SCHMITT, R.W. 1981 Form of the temperature-salinity relationship in the central water: evidence for double-diffusive mixing. *J. Phys. Oceanogr.* **11** (7), 1015–1026.
SCHMITT, R.W. 1988 Mixing in a thermohaline staircase. In *Elsevier Oceanography Series*, vol. 46, pp. 435–452. Elsevier.
SCHMITT, R.W. & EVANS, D.L. 1978 An estimate of the vertical mixing due to salt fingers based on observations in the north Atlantic central water. *J. Geophys. Res.-Oceans* **83** (C6), 2913–2919.
SCHMITT, R.W., LEDWELL, J.R., MONTGOMERY, E.T., POLZIN, K.L. & TOOLE, J.M. 2005 Enhanced diapycnal mixing by salt fingers in the thermocline of the tropical Atlantic. *Science* **308** (5722), 685–688.
SHEN, C.Y. 1989 The evolution of the double-diffusive instability: salt fingers. *Phys. Fluids* A **1** (5), 829–844.
SHEN, C.Y. 1995 Equilibrium salt-fingering convection. *Phys. Fluids* **7** (4), 706–717.
SHEN, C.Y. & VERONIS, G. 1997 Numerical simulation of two-dimensional salt fingers. *J. Geophys. Res.-Oceans* **102** (C10), 23131–23143.
SINGH, O.P. & SRINIVASAN, J. 2014 Effect of rayleigh numbers on the evolution of double-diffusive salt fingers. *Phys. Fluids* **26** (6), 062104.

SMITH, R., *et al.* 2010 The parallel ocean program (POP) reference manual: ocean component of the community climate system model (CCSM) and community earth system model (CESM). *LAUR-01853*, vol. 141, pp. 1–140.

ST. LAURENT, L. & SCHMITT, R.W. 1999 The contribution of salt fingers to vertical mixing in the North Atlantic tracer release experiment. *J. Phys. Oceanogr.* **29** (7), 1404–1424.

STELLMACH, S., TRAXLER, A., GARAUD, P., BRUMMELL, N. & RADKO, T. 2011 Dynamics of fingering convection. Part 2. The formation of thermohaline staircases. *J. Fluid Mech.* **677**, 554–571.

TRAXLER, A., STELLMACH, S., GARAUD, P., RADKO, T. & BRUMMELL, N. 2011 Dynamics of fingering convection. Part 1. Small-scale fluxes and large-scale instabilities. *J. Fluid Mech.* **677**, 530–553.

TURNER, J.S. 1967 Salt fingers across a density interface. In *Deep Sea Research and Oceanographic Abstracts*, vol. 14, pp. 599–611. Elsevier.

WALIN, G. 1964 Note on the stability of water stratified by both salt and heat. *Tellus* **16** (3), 389–393.

WELLS, M.G. & GRIFFITHS, R.W. 2003 Interaction of salt finger convection with intermittent turbulence. *J. Geophys. Res.-Oceans* **108** (C3).

WINTERS, K.B., LOMBARD, P.N., RILEY, J.J. & D'ASARO, E.A. 1995 Available potential energy and mixing in density-stratified fluids. *J. Fluid Mech.* **289**, 115–128.

ZHANG, J., SCHMITT, R.W. & HUANG, R.X. 1998 Sensitivity of the GFDL modular ocean model to parameterization of double-diffusive processes. *J. Phys. Oceanogr.* **28** (4), 589–605.